

000 001 002 003 004 005 006 007 008 009 010 011 012 013 014 015 016 017 018 019 020 021 022 023 024 025 026 027 028 029 030 031 032 033 034 035 036 037 038 039 040 041 042 043 044 045 046 047 048 049 050 051 052 053 ON THE INTERACTION OF COMPRESSIBILITY AND ADVERSARIAL ROBUSTNESS

Anonymous authors

Paper under double-blind review

ABSTRACT

Modern neural networks are expected to simultaneously satisfy a host of desirable properties: accurate fitting to training data, generalization to unseen inputs, parameter and computational efficiency, and robustness to adversarial perturbations. While compressibility and robustness have each been studied extensively, a unified understanding of their interaction still remains elusive. In this work, we develop a principled framework to analyze how different forms of structured compressibility - such as neuron-level sparsity and spectral compressibility - affect adversarial robustness. We show that these forms of compression can induce a small number of highly sensitive directions in the representation space, which adversaries can exploit to construct effective perturbations. Our analysis yields a robustness bound that reveals how neuron and spectral compressibility impact ℓ_∞ and ℓ_2 robustness via their effects on the learned representations. Crucially, the vulnerabilities we identify arise irrespective of how compressibility is achieved - whether via regularization, architectural bias, or implicit learning dynamics. Through empirical evaluations across synthetic and realistic tasks, we confirm our theoretical predictions, and further demonstrate that these vulnerabilities persist under adversarial training and transfer learning, and contribute to the emergence of universal adversarial perturbations. Our findings show a fundamental tension between structured compressibility and robustness and highlight new pathways for designing models that are both efficient and safe.

1 INTRODUCTION

Machine learning (ML) systems are increasingly deployed in high-stakes domains such as health-care (Rajpurkar et al., 2022) and autonomous driving (Hussain & Zeadally, 2019), where reliability is paramount. With their growing social impact, modern neural networks are now expected to meet a suite of often conflicting demands: they must fit the data (explain observations), generalize to unseen inputs, remain efficient in storage and inference, *i.e.*, be compressible, and exhibit robustness against adversarial perturbations, as well as other distribution shifts. While each of these desiderata has been studied extensively in isolation, a mature and unified understanding of how they interact - and in particular, how compressibility shapes robustness - remains elusive.

As desirable as adversarial robustness and compressibility both are, the research has been equivocal regarding whether/when/how their simultaneous achievement is possible (Guo et al., 2018; Balda et al., 2020; Li et al., 2020a; Merkle et al., 2022; Liao et al., 2022). This is even more pronounced for *structured* compressibility, which is alarming given its practical relevance (Blalock et al., 2020; Piras et al., 2025). However, recent research has started to provide mechanism-based explanations for this relationship, highlighting how compressibility impacts models' vulnerability to adversarial noise. For example, Savostianova et al. (2023) demonstrate that low-rank parameterizations may inadvertently amplify local Lipschitz constants, increasing sensitivity to perturbations. Nern et al. (2023) connect adversarial transferability to layer-wise operator norms and their impact on representation geometry. Feng et al. (2025) further shows that while moderate sparsity can enhance robustness, excessive sparsity causes ill-conditioning that reintroduces fragility and vulnerability. These results hint at a delicate, regime-dependent relationship between compressibility and robustness - but a principled and general framework is still lacking.

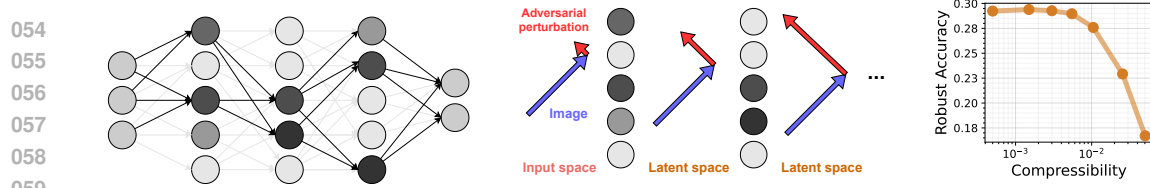


Figure 1: A visual preview of our findings. (Left) Sparsification expedites compression but creates sensitive latent directions. (Center) Adversaries exploit these sensitive directions to increase their potency. (Right) This leads to decreased adversarial robustness.

In this work, we develop a framework to investigate the effect of structured compressibility on adversarial robustness through its effect on parameter operator norms and network’s Lipschitz constant. We jointly study how different forms of compressibility - particularly neuron-level sparsity and spectral compression - affect adversarial robustness. Our central result is an instructive adversarial robustness bound that reveals how compressibility can induce a small set of highly sensitive directions in the representation space. These “adversarial directions” dramatically amplify perturbations and are readily exploited by adversaries. Empirically, we confirm that these axes are not merely theoretical constructs: adversarial attacks reliably identify and exploit them across architectures, datasets, and attack models. Figure 1 provides a visual preview of our findings. Previous research tightly links compressibility to generalization (Arora et al., 2018; Barsbey et al., 2021); however, our findings imply that the very mechanisms that promote generalization can also introduce structural weaknesses. In summary, our contributions are:

1. We provide an **adversarial robustness bound** that decomposes into analytically interpretable terms, and predicts that neuron and spectral compressibility create adversarial vulnerability against ℓ_∞ and ℓ_2 attacks, through their effects on networks’ Lipschitz constants.
2. Utilizing various compressibility-inducing interventions, we empirically validate our predictions regarding the **emergence of adversarial vulnerability under structured compressibility** with various datasets and models, including commonly used modern encoder architectures.
3. We demonstrate that the **detrimental effects of compressibility persist under adversarial training and transfer learning**, and contribute to the appearance of universal adversarial examples.
4. We demonstrate and discuss our findings’ implications for compression in practice, and highlight promising paths for **designing models that reconcile efficiency and safety**.

2 SETUP

Notation. We denote scalars by lower case italic (k), vectors with lower case bold (\mathbf{x}), and matrices with upper case bold (\mathbf{W}) characters respectively. Vector ℓ_p norms are denoted by $\|\mathbf{x}\|_p$. For matrices, $\|\mathbf{W}\|_F, \|\mathbf{W}\|_2, \|\mathbf{W}\|_\infty$ correspond to Frobenius, spectral, and ℓ_∞ operator norms, respectively. We denote the i^{th} element of a vector \mathbf{x} with x_i , and row i of a matrix \mathbf{W} with \mathbf{w}_i . Elements of a sequence of matrices (e.g. layer matrices) are referred to by $\mathbf{W}^l, l \in [\lambda]$. For an integer n , we use $[n] := (1, \dots, n)$.

Unless otherwise specified, we will be focusing on supervised classification problems, which will involve the input $\mathbf{x} \in \mathcal{X}$ and label $y \in \mathcal{Y}$. A predictor $g : \mathcal{X} \rightarrow \mathbb{R}^{|\mathcal{Y}|}$, parametrized by $\boldsymbol{\theta} \in \Theta$ produces output logits $\mathbf{s} = g(\mathbf{x}, \boldsymbol{\theta})$, the maximum of which is the predicted label $\hat{y} = \arg \max_{i \in |\mathcal{Y}|} s_i$. Predictions are evaluated by a loss function $\ell : \mathbb{R}^{|\mathcal{Y}|} \times \mathcal{Y} \rightarrow \mathbb{R}_+$. For brevity, we define the composite loss function $f(\mathbf{x}, \boldsymbol{\theta}) := \ell(g(\mathbf{x}, \boldsymbol{\theta}), y)$.

Risk and adversarial robustness. Assuming a data distribution π on $\mathcal{X} \times \mathcal{Y}$, we define the population and empirical risks accordingly: $F(\boldsymbol{\theta}) := \mathbb{E}_{\mathbf{x}, y \sim \pi}[f(\mathbf{x}, \boldsymbol{\theta})]$, and $\widehat{F}(\boldsymbol{\theta}, S) := \frac{1}{n} \sum_{i=1}^n f(\mathbf{x}_i, \boldsymbol{\theta})$, where $(\mathbf{x}_i, y_i)_{i=1}^n$ denotes a set of i.i.d. samples from π . Adversarial attacks are minimal perturbations to input that dramatically disrupt a model’s predictions (Szegedy et al., 2014). In this paper, we focus on bounded p -norm attacks, which we define as

$$\mathbf{a}^* = \arg \max_{\|\mathbf{a}\|_p \leq \delta} f(\mathbf{x} + \mathbf{a}, \boldsymbol{\theta}). \quad (1)$$

Given the adversarial loss $f_p^{\text{adv}}(\mathbf{x}, \boldsymbol{\theta}; \delta) := f(\mathbf{x} + \mathbf{a}^*, \boldsymbol{\theta})$, we define adversarial risk and empirical adversarial risk as $F_p^{\text{adv}}(\boldsymbol{\theta}; \delta) := \mathbb{E}_{\mathbf{x}, y \sim \pi}[f_p^{\text{adv}}(\mathbf{x}, \boldsymbol{\theta}; \delta)]$ and $\widehat{F}_p^{\text{adv}}(\boldsymbol{\theta}, S; \delta) := \frac{1}{n} \sum_{i=1}^n f_p^{\text{adv}}(\mathbf{x}_i, \boldsymbol{\theta}; \delta)$,

108 respectively. The *attack norm* p chosen under the *attack budget* δ determines the type of adversarial
 109 attack in question, with $p = 2$ and $p = \infty$ as the most common choices. In this paper, we are
 110 primarily interested in what we call the *adversarial robustness gap*: $\Delta_p^{\text{adv}} := F_p^{\text{adv}}(\boldsymbol{\theta}, \delta) - F(\boldsymbol{\theta})$. A
 111 model with small Δ_p^{adv} is considered *adversarially robust*.
 112

113 **Neural networks.** Our analyses will focus on neural networks under classification. We define a fully
 114 connected neural network (FCN) with λ hidden layers of h units as below:

$$115 \quad g(\mathbf{x}, \boldsymbol{\theta}) = \mathbf{C}\phi(\mathbf{W}^\lambda\phi(\dots\mathbf{W}^1\mathbf{x})), \quad (2)$$

117 where $\boldsymbol{\theta} := (\mathbf{C}, \mathbf{W}^1, \dots, \mathbf{W}^\lambda)$, \mathbf{W}^l and \mathbf{C} denote hidden layer and linear classification head
 118 parameters respectively, and ϕ is elementwise ReLU activation function. We omit $\boldsymbol{\theta}$ when it is
 119 obvious from the context for brevity. We can write g as the composition of two functions, a
 120 linear classifier head $c : \mathbb{R}^h \rightarrow \mathbb{R}^{|\mathcal{Y}|}$, and a feature encoder $\Phi : \mathcal{X} \rightarrow \mathbb{R}^h$, such that $g(\mathbf{x}, \boldsymbol{\theta}) :=$
 121 $c(\cdot, \mathbf{C}) \circ \Phi(\cdot, \mathbf{W}^1 \dots \mathbf{W}^\lambda)(\mathbf{x})$. When needed, we use $\mathbf{z} = \Phi(\mathbf{x})$ or $\mathbf{z}_{\text{adv}} = \Phi(\mathbf{x}_{\text{adv}})$ to denote latent
 122 representations, where $\mathbf{x}_{\text{adv}} := \mathbf{x} + \mathbf{a}^*$. To avoid notational clutter and without loss of generality,
 123 throughout our analyses we assume that $\mathbf{x} \in \mathbb{R}^h$, and omit bias parameters.
 124

125 **Lipschitz continuity.** Given two L^p spaces \mathcal{X} and \mathcal{Y} , a function $g : \mathcal{X} \rightarrow \mathcal{Y}$ is called Lipschitz
 126 continuous if there exists a constant K_p such that $\|g(\mathbf{x}^1) - g(\mathbf{x}^2)\|_p \leq K_p \|\mathbf{x}^1 - \mathbf{x}^2\|_p$, $\forall \mathbf{x}^1, \mathbf{x}^2 \in \mathcal{X}$.
 127 Said K_p is called the (global) Lipschitz constant. Any K_p that is valid for a subspace $\mathcal{U} \subset \mathcal{X}$ is
 128 called a local Lipschitz constant. Although its computation is NP-hard for even the simplest neural
 129 networks (Scaman & Virmaux, 2018); as a notion of input-based volatility, estimation, utilization,
 130 and regularization of the Lipschitz constant have been a staple of robustness research (Cisse et al.,
 131 2017; Bubeck et al., 2020; Muthukumar & Sulam, 2023; Grishina et al., 2025). Note that the FCN
 132 as defined in (2) is Lipschitz continuous in ℓ_p for $p \in [2, \infty]$, along with other commonly used
 133 architectures such as convolutional neural networks (CNN) (Zühlke & Kudenko, 2025).

134 **Compressibility.** Various prominent approaches to neural network compression exist, such as
 135 pruning, quantization, distillation, and conditional computing, (O’Neill, 2020). Here we focus on
 136 pruning and low-rank approximation, two of the most commonly used and researched forms of
 137 compression (Hohman et al., 2024). More specifically, we focus on inherent properties of network
 138 parameters that make them amenable to pruning or low-rank approximation, i.e. their *compressibility*.
 139 We will first present a formal definition of a *compressible* vector, and then will show how this
 140 definition can be utilized to describe both structured prunability and low-rankness.

141 **Definition 2.1** ((q, k, ϵ)-compressibility). *Given a vector $\boldsymbol{\theta} \in \mathbb{R}^d$ and a non-negative integer $k \leq d$,
 142 let $\boldsymbol{\theta}_k$ denote the compressed vector which contains the largest (in magnitude) k elements of $\boldsymbol{\theta}$ with
 143 all the other elements set to 0. Then, $\boldsymbol{\theta}$ is (q, k, ϵ) -compressible if and only if*

$$144 \quad \|\boldsymbol{\theta} - \boldsymbol{\theta}_k\|_q / \|\boldsymbol{\theta}\|_q \leq \epsilon. \quad (3)$$

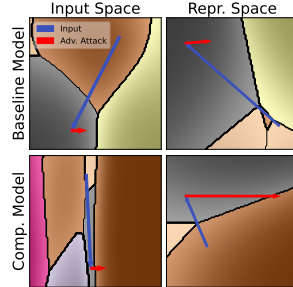
145 In the case of equality, we call $\boldsymbol{\theta}$ to be strictly (q, k, ϵ) -compressible. Complementarily, the spread
 146 variable $\beta \in [0, 1]$ can be used to characterize the dispersion of top- k terms, such that $|\theta_{m_k}| =$
 147 $(1 - \beta)|\theta_{m_1}|$, where m_i indexes the i ’th largest magnitude element in the vector.
 148

149 Moving forward we will assume any vector denoted as compressible is strictly compressible, unless
 150 otherwise noted. See the Appendix for a more in-depth discussion of our compressibility definition
 151 and how it relates to other notions of approximate sparsity, where we show that our definition distin-
 152 guishes qualitatively different parameter configurations better compared to prominent alternatives.
 153

154 **Structured compressibility.** Importantly, given that the $\boldsymbol{\theta}$ can be any vector, the above definition can
 155 be used flexibly to describe different notions of compressibility, including those of structured com-
 156 pressibility, where particular substructures in the model dominate the rest. More specifically, given a
 157 layer parameter matrix $\mathbf{W} \in \mathbb{R}^{h \times h}$ from (2), let $\boldsymbol{\nu} := (\|\mathbf{w}_1\|_1, \dots, \|\mathbf{w}_h\|_1)$ denote ℓ_1 norms of rows
 158 of the matrix \mathbf{W} . The compressibility of $\boldsymbol{\nu}$ would correspond to *row/neuron compressibility*, which is
 159 a desirable property for neural network parameters as it expedites pruning of whole neurons, with tan-
 160 gible computational gains. Note that this also would correspond to filter compressibility/prunability
 161 in CNNs with a matricization of the convolution tensor. Similarly, let $\boldsymbol{\sigma} := (\sigma_1, \sigma_2, \dots)$ denote the
 162 singular values of matrix \mathbf{W} . Compressibility of $\boldsymbol{\sigma}$ would correspond to *spectral compressibility*,
 163 serving as a notion of approximate/numerical low-rankness.

162 3 NORM-BASED ADVERSARIAL ROBUSTNESS BOUNDS
163

164 **Motivating hypothesis.** Our analysis relies on a fundamental intuition: Although structured
165 (neuron, spectral) compressibility is desirable from a computational perspective, it also fo-
166 cuses the total energy of the parameters on a few dominant terms (rows/filters, singular values).
167 This in turn creates a few, potent directions in the latent space and increases the operator norms of the parameters (ℓ_∞ , ℓ_2 operator norms
168 respectively). This increases their sensitivity to worst-case perturbations: adversarial attacks exploiting these directions are amplified in
169 the representation space, and can more easily disrupt the predictions of the model. For a more specific example using spectral compressibility,
170 given a single layer neural network $g(\mathbf{x}) = \mathbf{C}\phi(\mathbf{W}\mathbf{x})$, assume that
171 $\sigma_1 \gg \sigma_{j \neq 1}$, i.e. first SV dominates the remaining singular values
172 as a result of high compressibility. Then, an adversarial perturbation \mathbf{a} that “aligns” with the associated right singular vector \mathbf{v}_1 s.t.
173 $\mathbf{v}_1^T \mathbf{a} / \|\mathbf{a}\|_2 \approx 1$, will have multiplied their post-layer representation
174 by $\sim \sigma_1$. This in turn would allow them to dominate the latent space
175 against the original image, i.e. increase $\|\mathbf{z}_{\text{adv}} - \mathbf{z}\|_2 / \|\mathbf{z}\|_2$, and ultimately change the prediction of the model. Taken from an experiment
176 presented in full detail in Section 4, Figure 2 visualizes this phenomenon in reality. Here, we utilize
177 PCA to visualize the input image, adversarial perturbation, and decision boundaries for a single
178 sample under a baseline vs. compressible (low-rank) model. The top row visualizes the baseline
179 model, where the minuscule adversarial perturbation fails to move the perturbed image across class
180 boundaries. The bottom row however, illustrates the compressible model under attack. Here, although
181 attack budget is identical in the input space, the adversarial perturbation is dramatically amplified in
182 the representation space, leading to a successful adversarial attack. Note that the decision boundaries
183 in compressible model’s input space is much more contracted to reflect this vulnerability. In the
184 Appendix, we dedicate a section to providing a stronger, step-by-step intuition for our hypotheses.
185

186 Figure 2: Decision boundaries under compressibility.
187

188 **Compressibility-based Lipschitz bounds.** Our theory will relate structured compressibility to
189 robustness through its effect on the network’s operator norms and Lipschitz constants. However,
190 this brings about a particular conceptual challenge. Our notion of (q, k, ϵ) -compressibility, like
191 others’ (Diao et al., 2023), is a *scale-independent* measure. Therefore, any direct relation between
192 compressibility and Lipschitz constants would be rendered void by the arbitrary scaling of the
193 parameters. Therefore, we characterize ℓ_∞ and ℓ_2 operator norms of the parameters by an upper
194 bound that decomposes into (compressibility \times Frobenius norm) terms. This “structure vs. scale”
195 decomposition allows us to meaningfully relate compressibility and robustness, and also allows us to
196 develop concrete hypotheses regarding the effect of various interventions in neural network training.
197

198 **Theorem 3.1.** *The following statements relate operator norms and structured compressibility.*
199

200 **(a) Neuron compressibility (i.e. row-sparsity):** Let $\mathbf{w}_i, i \in [h]$ denote the rows of the matrix \mathbf{W} , and
201 let $\boldsymbol{\nu} := (\|\mathbf{w}_1\|_1, \dots, \|\mathbf{w}_h\|_1)$ denote ℓ_1 norms of its rows. Assuming $\boldsymbol{\nu}$ is $(1, k_{\boldsymbol{\nu}}, \epsilon_{\boldsymbol{\nu}})$ compressible
202 and each row \mathbf{w}_i is $(2, k_r, \epsilon_r)$ -compressible implies:

$$\|\mathbf{W}\|_\infty \leq \frac{(1 - \epsilon_{\boldsymbol{\nu}})}{(1 - \beta_{\boldsymbol{\nu}})} \left(\frac{\sqrt{hk_r} + h\epsilon_r}{k_{\boldsymbol{\nu}}} \right) \|\mathbf{W}\|_F. \quad (4)$$

203 **(b) Spectral compressibility (i.e. low-rankness):** Let $\boldsymbol{\sigma} := (\sigma_1, \sigma_2, \dots)$ denote the singular values
204 of matrix \mathbf{W} . Assuming $\boldsymbol{\sigma}$ is $(1, k_{\boldsymbol{\sigma}}, \epsilon_{\boldsymbol{\sigma}})$ -compressible implies:

$$\|\mathbf{W}\|_2 \leq \frac{(1 - \epsilon_{\boldsymbol{\sigma}})}{(1 - \beta_{\boldsymbol{\sigma}})} \left(\frac{\sqrt{h}}{k_{\boldsymbol{\sigma}}} \right) \|\mathbf{W}\|_F. \quad (5)$$

205 Intuitively, Theorem 3.1 describes how increasing compressibility affects layer operator norms:
206 Neuron compressibility, i.e. a small number of rows dominating the matrix increases ℓ_∞ operator
207 norm of the matrix, especially if the spread within these dominant rows are high. Similarly, increased
208 spectral compressibility and spread increases the ℓ_2 operator norm. Note that the latter result is
209 closely related to results from the literature that connect stable rank or condition number to robustness
210 (Savostianova et al., 2023; Feng et al., 2025), see Section 5. We highlight that although Theorem 3.1
211 directly relates neuron and spectral compressibility to perturbations defined in ℓ_∞ and ℓ_2 norms, we
212

216 do not claim that relationships across attack and operator norms do not hold. Indeed in our Appendix,
 217 we show that the two operator norms are likely to move together under compressibility, connecting
 218 structured compressibility to a broader notion of adversarial vulnerability. Lastly, while we utilize
 219 the upper bounds for our following theoretical results, additional theoretical results in the Appendix
 220 characterize lower bounds on the operator norm with similar implications.

221 As we move on to characterizing layers within a neural network, \mathbf{W}_k^l will be used to denote the
 222 *compressed* version of the parameter matrix of layer l . In the case of row compression, this will
 223 correspond to keeping the k dominant rows as is, and setting the $h - k$ trailing rows to $\mathbf{0}$. In the
 224 case of spectral compression, given the singular value decomposition (SVD), $\mathbf{W}^l = \mathbf{U}^l \Sigma^l \mathbf{V}^{l^T}$, the
 225 compressed matrix would correspond to $\mathbf{W}_k^l := \mathbf{U}_k^l \Sigma_k^l \mathbf{V}_k^{l^T}$, where the $h - k$ smallest singular values
 226 are truncated.

227 Note that the sensitivity of the network not only relies on the characteristics of layer parameters, but
 228 also on the interactions between them. For example, it is possible to upper bound the operator norm
 229 of two consecutive layers interleaved by a ReLU nonlinearity with $\|\mathbf{W}^{l+1}\| \|\mathbf{W}^l\|$. However, this
 230 is an overly pessimistic bound, as it accounts for the most potent directions of each layer perfectly
 231 lining up (unlikely in reality), and ignores the nonlinearity (Scaman & Virmaux, 2018). This is why
 232 for our following theorem, we first introduce the interlayer alignment terms A_p : These terms will
 233 help compute a more realistic joint operator norm across layers by correcting for the said overly
 234 pessimistic assumption by using the “alignment” of the top- k terms in each layer. With \mathcal{D} as the set
 235 of all diagonal binary matrices representing ReLU activations, we define A_p for $p \in \{2, \infty\}$ as:

$$237 \quad A_\infty(l) \triangleq \max_{\mathbf{D} \in \mathcal{D}} \frac{\|\mathbf{W}_k^{l+1} \mathbf{D} \mathbf{W}_k^l\|_\infty}{\|\mathbf{W}^{l+1}\|_\infty \|\mathbf{W}^l\|_\infty} + R_\infty(\epsilon) \quad (6)$$

$$239 \quad A_2(l) \triangleq \max_{\mathbf{D} \in \mathcal{D}} \frac{\|\sqrt{\Sigma_k^{l+1} \mathbf{V}_k^{l+1^T} \mathbf{D} \mathbf{U}_k^l \sqrt{\Sigma_k^l}}\|_2}{\sqrt{\|\mathbf{W}^{l+1}\|_2 \|\mathbf{W}^l\|_2}} + R_2(\epsilon), \quad (7)$$

243 where R_∞, R_2 are remainder alignment terms defined and shown to be $R_p(\epsilon) \rightarrow 0$ as $\epsilon \rightarrow 0$ in the
 244 Appendix for brevity. We refer the reader to our proofs in the Appendix to explain the exact form the
 245 alignment terms take and a comparison to previous approaches (Scaman & Virmaux, 2018), where
 246 we also dedicate a section to provide a more intuitive understanding for them. Having Theorem 3.1
 247 to help characterize the compressibility-based sensitivity of layers, and (6) and (7) to help connect
 248 them, we now provide an upper bound to the Lipschitz constant of the complete encoder network.

249 **Theorem 3.2.** Let L_Φ^p be the Lipschitz constant of the encoder Φ defined following (2). Let \mathcal{D} denote
 250 the set of all diagonal binary matrices, corresponding to ReLU activation layers. Then:

251 (a) **Neuron compressibility:** The ℓ_∞ Lipschitz constant of Φ can be upper bounded by:

$$253 \quad L_\Phi^\infty \leq \hat{L}_\Phi^\infty := \prod_{l=1}^{\lambda} \frac{(1 - \epsilon_\nu)}{(1 - \beta_\nu)} \left(\frac{\sqrt{hk_r} + h\epsilon_r}{k_\nu} \right) \|\mathbf{W}^l\|_F \prod_{l=1}^{\lambda-1} \tilde{A}_\infty(l), \quad (8)$$

256 where $\tilde{A}_\infty(l) = A_\infty(l)$ if $l \in S_{opt}$, and 1 otherwise. $S_{opt} \subseteq \{1, 2, \dots, \lambda - 1\}$ is the optimal
 257 alignment partition set (See Definition A.4) that can be determined in $O(\lambda)$ time.

258 (b) **Spectral compressibility:** The ℓ_2 Lipschitz constant of Φ can be upper bounded by:

$$260 \quad L_\Phi^2 \leq \hat{L}_\Phi^2 := \prod_{l=1}^{\lambda} \frac{(1 - \epsilon_\sigma)}{(1 - \beta_\sigma)} \left(\frac{\sqrt{h}}{k_\sigma} \right) \|\mathbf{W}^l\|_F \prod_{l=1}^{\lambda-1} A_2(l). \quad (9)$$

263 We note that this upper bound can be directly used in conjunction with other results from the literature
 264 (Ribeiro et al., 2023) to characterize adversarial robustness gap:

266 **Corollary 3.3.** Under a binary classification task with cross-entropy loss, $\ell(y, \mathbf{x}^\top \boldsymbol{\theta}) = \ell(y, \hat{y}) =$
 267 $\log(1 + e^{-y\hat{y}})$, given a neural network classifier as described in (2), under the same assumptions
 268 with (8), $F_\infty^{\text{adv}}(\boldsymbol{\theta}; \delta) \leq F(\boldsymbol{\theta}) + \delta \hat{L}_\Phi^\infty \|\boldsymbol{\theta}\|_1$. Similarly, under the assumptions of (9), we have
 269 $F_2^{\text{adv}}(\boldsymbol{\theta}; \delta) \leq F(\boldsymbol{\theta}) + \delta \hat{L}_\Phi^2 \|\boldsymbol{\theta}\|_2$.

270 Note that although bounds provided in Theorem 3.2 are tighter than the
 271 pessimistic ‘‘product-of-norms’’ bounds, it deliberately *trades off* some
 272 tightness by utilizing Theorem 3.1. However, in return, this results in
 273 a bound that decomposes into analytically interpretable and actionable
 274 terms. Such bounds have proven valuable in analyzing adversarial
 275 robustness in deep learning (Wen et al., 2020). Regardless, Figure 3
 276 demonstrates the close correlation our bound shows with the empirical
 277 robustness gap ($\rho = 0.947$), in a 2-hidden-layer neural network
 278 with varying spectral compressibility (obtained through systematically
 279 varying the rank of factorized layer matrices). We provide full details
 280 in the Appendix, where we also show that as the global Lipschitz constant increases, empirically
 281 estimated local Lipschitz constants scale accordingly. There, we also explore the alignment terms’
 282 empirical behavior and estimation techniques, although a detailed analysis thereof lies beyond our
 283 primary focus. We now translate these theoretical insights into concrete hypotheses and test them
 284 through experiments.

285 4 EXPERIMENTAL EVALUATION

287 We now validate our theoretical findings through systematic experimentation. We first validate our
 288 *motivating hypothesis* and then empirically show that (i) neuron and spectral compressibility-inducing
 289 interventions will reduce adversarial robustness against ℓ_∞ and ℓ_2 adversarial attacks; (ii) the negative
 290 effects of compressibility to persist under adversarial training, (iii) the compressibility-related vulner-
 291 abilities being baked into the learned representations during pretraining, will impact any downstream
 292 task in transfer learning; (iv) increasing compressibility creates vulnerable directions in the latent
 293 space, further enabling universal adversarial examples (UAEs), while increasing Frobenius norm will
 294 create vulnerability without leading to UAEs; and (v) compressed models will inherit the vulnerability
 295 of the original models, and conducting compression based on (q, k, ϵ) -compressibility, reducing the
 296 spread of the dominant terms, or regularizing interlayer alignment will improve robustness.

297 **Datasets, architectures, and training.** We conduct our experiments in the most commonly used
 298 datasets and architectures in the literature on adversarial robustness and compression (Piras et al.,
 299 2025). Datasets we use include MNIST (Deng, 2012), CIFAR-10, CIFAR-100 (Krizhevsky & Hinton,
 300 2009), SVHN (Netzer et al., 2011), Flickr30k (Young et al., 2014), and ImageNet-1k (Deng et al.,
 301 2009). Architectures we utilize include fully connected networks (FCN), ResNet18 (He et al., 2016),
 302 VGG16 (Simonyan & Zisserman, 2014), WideResNet-101-2 (Zagoruyko & Komodakis, 2016), vision
 303 transformer (ViT) - both as a standalone classifier (Dosovitskiy et al., 2021) and as part of a CLIP
 304 encoder (Radford et al., 2021), and Swin Transformer (Liu et al., 2021). Unless otherwise noted, we
 305 use softmax cross-entropy loss, the AdamW optimizer with a weight decay of 0.01, a learning rate of
 306 0.001, and use a validation set based model selection for early stopping. See the associated code base
 307 for additional implementation details, to be made publicly available upon publication.

308 **Evaluating and training for adversarial robustness.** When evaluating adversarial robustness, we
 309 utilize AutoPGD as the primary adversarial attack algorithm for evaluation (Croce & Hein, 2020),
 310 as implemented by Nicolae et al. (2018). When training for adversarial robustness, we utilize a
 311 PGD attack to generate adversarial samples at every iteration (Madry et al., 2018). Unless otherwise
 312 noted, we use a ratio of 0.5 for adversarial samples in a training minibatch. We use $\epsilon = 8/255$ and
 313 $\epsilon = 0.5$ for ℓ_∞ and ℓ_2 attacks respectively for end-to-end adversarially trained models. We use
 314 $0.25 \times$ of these budgets for evaluating standard trained or adversarially fine-tuned models to allow a
 315 visible comparison (See Appendix for qualitatively identical results under different budgets and [attack
 316 algorithms](#)). By default, we present results for ℓ_∞ and ℓ_2 attacks when evaluating robustness under
 317 neuron and spectral compressibility respectively, and defer the cross-norm results to the supplementary
 318 material, which also includes further details on our experiment settings and implementation.

319 **Comparison across methods.** Given that our theory is agnostic to the source of structured compress-
 320 ibility, we experiment and confirm our predictions with various methods to induce compressibility.
 321 Therefore, to retain the equivalence between these different methods and prevent confounding from
 322 specific compression procedures, we primarily compare uncompressed models while explicitly high-
 323 lighting their different levels of compressibility. However, in approaches where a specific compression
 324 procedure is commonly utilized in practice (e.g. filter pruning after regularized training), we show
 325 that our results apply to the compressed models as well.

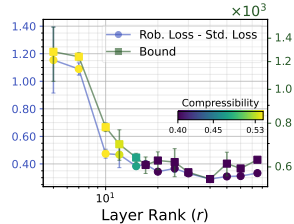
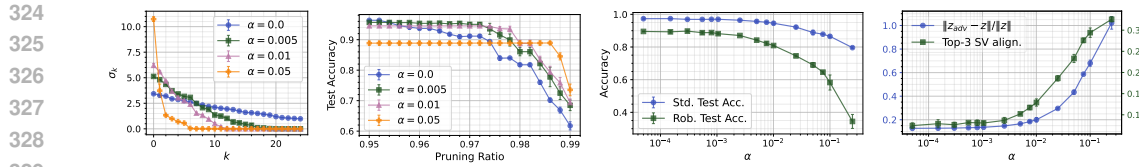


Figure 3: Corollary 3.3 vs. empirical robustness gap.

Figure 4: Model statistics under increasing strength of nuclear norm regularization (α).

4.1 RESULTS

Testing the motivating hypothesis. We start our empirical analysis with a demonstrative experiment to visually investigate the implications of our motivating hypothesis. For this, we train a single 400-width hidden layer FCN with ReLU activations on the MNIST dataset. We use nuclear norm regularization (NNR) to encourage spectral compressibility, adding the term $\alpha \|\sigma\|_1$ to the training objective, with α as a hyperparameter. To avoid confounding by NNR decreasing overall parameter norms, we apply Frobenius norm normalization to \mathbf{W}^1 at every iteration (Miyato et al., 2018). **While our following experiments will utilize more practically relevant norm control mechanisms, we currently apply normalization to fully isolate the effects of compressibility.**

In Figure 4 (left) we validate that our intervention indeed increases spectral norm compressibility. As expected, Figure 4 (center left) shows that spectral compressibility actually allows pruning: the more compressible models retain their performance under stronger spectral pruning. Figure 4 (center right) shows that increased compressibility comes at the cost of adversarial robustness: as α increases, adversarial accuracy dramatically falls. We further investigate whether this fall is due to our hypothesized mechanism. **As in our motivating hypothesis at the beginning of Section 3**, we let $\mathbf{z} = \Phi(\mathbf{x})$ and $\mathbf{z}_{\text{adv}} = \Phi(\mathbf{x} + \mathbf{a}^*)$ denote the learned representations of clean and perturbed input images. If the adversarial attacks are taking advantage of the potent directions created by compressibility, then as compressibility increases: (1) The perturbations \mathbf{a}^* should align more with the dominant singular directions, *i.e.*, $\mathbf{v}_i^\top \mathbf{a}^* \gg \mathbf{v}_j^\top \mathbf{a}^* \forall i \in [k], j \notin [k]$, (2) representations of adversarial perturbations should grow stronger in relation to the original image's representation, *i.e.* $\|\mathbf{z}_{\text{adv}} - \mathbf{z}\|_2 / \|\mathbf{z}\|_2$ should increase. Results presented in Figure 4 (right) confirms both predictions, further supporting our motivating hypothesis. Lastly, the previously presented Figure 2 visualizes the effect of compressibility in the input and representation space. **We provide a more detailed, step-by-step account of how potent leading directions are exploited by white box and black box adversaries in the Appendix for stronger intuition.**

Adversarial robustness and compressibility under standard training. For implications of our analysis under more realistic settings, we start by investigating the effects of compressibility on adversarial robustness in fully connected networks (FCN). We induce neuron and spectral compressibility through group lasso regularization¹ and low-rank factorization, respectively (latter avoids the excessive cost of nuclear norm regularization). As above, we conduct Frobenius norm normalization at every iteration. Figure 5 (top) presents the results of these experiments: The reduction in adversarial robustness as a function of increasing compressibility is clear in both cases, confirming our main hypothesis. Note that we present robust accuracy (RA) / standard accuracy (SA) ratio alongside RA to highlight that the obtained results are not due to baseline SA being lower under compressibility.

We then investigate whether our hypotheses apply beyond the context of our theory, starting with convolutional neural networks (CNNs). We first test our predictions in ResNet18 models trained on CIFAR-10 datasets. Here we eschew Frobenius norm normalization for standard weight decay.

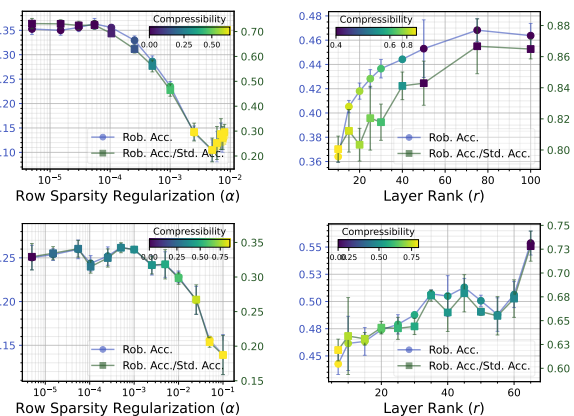


Figure 5: Results with FCN (top) and ResNet18 (bottom) trained on CIFAR-10 dataset.

¹Group lasso regularization penalizes the ℓ_1 norm of row ℓ_2 norms of each layer, promoting row-sparsity.

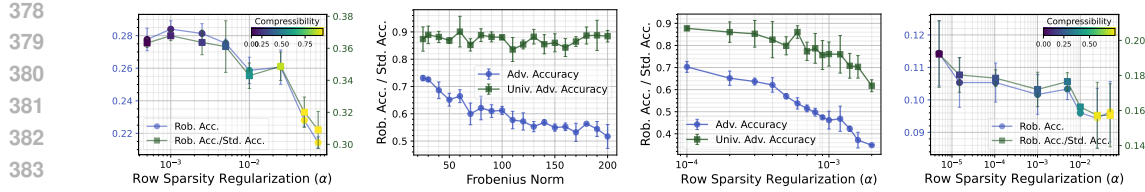


Figure 7: (Left) Effects of compressibility under adversarial training. UAEs under increasing (center left) compressibility vs. (center right) parameter scale. (Right) Robustness under transfer learning.

However, to prevent confounding from group lasso’s effect on general parameter scales, we create a scale-invariant version that regularizes row norms’ ℓ_1/ℓ_2 norm ratio.² Figure 5 (bottom) demonstrates that the above effects clearly translate to this setting as well, further solidifying the relationship between structured compressibility and adversarial robustness. We present similar results on two other architectures (VGG16, WideResNet-101) and two other datasets (CIFAR-100, SVHN) in the Appendix. Going forward, for brevity we will focus on neuron compressibility results, and defer corresponding spectral compressibility results to the Appendix, where we also discuss unstructured compressibility and inductive bias-based emergent compressibility.

Experiments with transformers. We next test our hypotheses under transformer architectures. Figure 6 (left) replicates our results under a ViT classifier model trained on CIFAR-10 dataset. Further, to test whether our hypothesis holds under a zero-shot classification setting, we fine-tune a pre-trained CLIP model on Flickr30k dataset under varying degrees of sparsification regularization, and conduct standard and adversarial zero-shot classification using ImageNet-1k dataset. We find that our results (Figure 6, right) replicate here as well. That simply fine-tuning with sparsification can create this vulnerability with commonly repurposed encoder backbones highlights the safety implications of our results. See Appendix for further details and findings under other training settings.

Effects of compressibility on robustness under adversarial training. Given that adversarial training is the primary method for obtaining models that are robust against adversaries, we next investigate whether the effects we have observed will persist under this regime. To make this setting as close to practice as possible, we also include a learning rate annealing schedule (Cosine annealing) and basic data augmentation (random horizontal flip and crops). The results almost identically replicate our observations under standard training (Figure 7, left). Although adversarial training increases adversarial robustness overall, the relative effect of compressibility remains as it is.

Universal adversarial examples. Examining the terms in Theorem 3.2, we predict that while both compressibility and Frobenius norm are likely to increase vulnerability, only the former is likely to lead to universal adversarial examples (UAEs) (Moosavi-Dezfooli et al., 2017), due to the global vulnerable directions it creates. To test our hypothesis, we modify the setting of FCN experiments presented above: In contrast to increasing row sparsity regularization under a fixed Frobenius norm, in an alternative set of experiments we systematically increase the constant to which Frobenius norm of the layers is fixed, without any row sparsity regularization. We utilize a FGSM-based (Goodfellow et al., 2015) UAE computation to develop adversarial samples. Figure 7 (center left, center right) confirms our hypothesis: while increasing Frobenius norm only decreases standard adversarial robustness, increasing compressibility *additionally* creates vulnerability to UAEs. [In the Appendix, we replicate these results under a ResNet18. Importantly, we also show that the converse relationship also holds: Training against UAEs vs. standard adversarial samples decreases top- \$k\$ parameter spread \$\beta\$, providing further support for our arguments.](#)

Adversarial vulnerability under transfer learning. Next, we investigate our hypothesis that the effects of compressibility should persist under transfer learning due to the structural effects created on representations. We train a ResNet18 model on CIFAR-100 dataset with increasing row sparsity regularization. After the training is complete, we freeze the encoder parameters and train a linear

²In the Appendix, we show that standard group lasso creates a “tug-of-war” between increasing compressibility and decreasing parameter scales; the former eventually wins, resulting in decreased robustness.

432 classifier head for prediction on CIFAR-10 dataset and evaluate the robustness of the resulting
 433 model. Figure 7 (right) shows that the effects of compressibility observed above directly translate
 434 to the context of transfer learning, where increased compressibility in pretraining affects robustness
 435 performance in the downstream task, for which the network is fine-tuned.

436 **Compression and robustness.** We now investigate the behavior of models under layerwise filter
 437 pruning. Using the ResNet18 and CIFAR-10 combination under adversarial training, in Figure 8
 438 (left), we compare the baseline model ($\alpha = 0.0$) to a model regularized to be compressible ($\alpha = 0.1$).
 439 We see that at no point the compressed models surpass the uncompressed performance of the baseline
 440 model in terms of standard and robust accuracy. However, as pruning ratio increases, the baseline model fails
 441 to retain its standard and robust performance, whereas the compressible (sparsified) model does considerably
 442 better, demonstrating the fundamental tension between robustness and compressibility. **In the Appendix, we show that these results hold after post-pruning fine-tuning as well.**
 443 Additionally, there we demonstrate that post-pruning fine-tuning acts as an additional source of
 444 vulnerability in and of itself, as under this procedure adversarial robustness deteriorates much faster
 445 than standard accuracy, confirming our results under yet another source of norm imbalance.
 446

447 In Figure 8 (right), we show that conducting pruning based on two simple interventions inspired
 448 by our bounds results in tangible improvements in standard and robust performance under pruning.
 449 Given the fact that layerwise pruning is known to produce harmful bottlenecks that lead to layer
 450 collapse (Blalock et al., 2020), instead of targeting a pruning ratio and pruning each layer accordingly,
 451 we set a target ϵ for each layer, and for each compute k that satisfies this ϵ level. Given a target
 452 global pruning ratio, we scan over different levels of ϵ and determine the level that gets closest
 453 to the target ratio. Moreover, during training we control the spread of the dominant terms, β ,
 454 which our analyses show to be harmful for robustness, without decreasing compressibility. We
 455 accomplish this through regularizing the variance of the top 0.05 of each layer’s filters’ norms.
 456 Figure 8 (right) demonstrates that our interventions create a tangible improvement in performance
 457 retention. **In the Appendix, we provide additional results showing that interlayer alignment can**
 458 **also be successfully used as a regularization target for robust compressibility.** We consider these
 459 interventions both as validations of our theory and promising directions for future robust compression
 460 research. However, we also highlight that it may not be possible to completely negate the fundamental
 461 dangers of concentrating parameter energy in very few substructures, extensively demonstrated by
 462 our theory and experiments. Therefore, while pruning and low-rank approximation remain valuable
 463 compression methods, combining intermediate levels thereof with other compression methods such
 464 as quantization or knowledge distillation seems to be the most promising approach in reconciling
 465 safety and robustness, which is in line with recent findings in the literature (Pavlitska et al., 2023).
 466

467

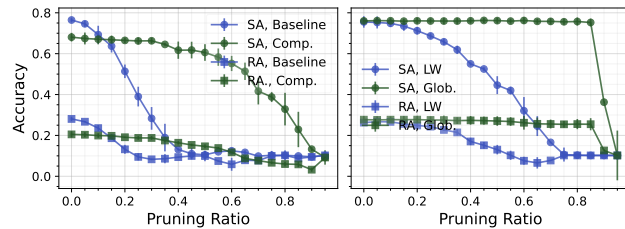
472 5 RELATED WORK

473

474 **Adversarial robustness.** The susceptibility of the neural network models to adversarial examples
 475 created through small perturbations (Szegedy et al., 2014) engendered a lot of research investigating
 476 the issue (Madry et al., 2018). To this day adversarial robustness remains one of the most important
 477 topics in machine learning safety (Malik et al., 2024). The literature ranges from the development
 478 of new attacks and defenses (Moosavi-Dezfooli et al., 2016; Abdollahpoorrostam et al., 2024), to
 479 investigating sources/mechanisms of adversarial vulnerability, to implications of AEs for the inductive
 480 biases of modern machine learning architectures (Ilyas et al., 2019; Ortiz-Jimenez et al., 2021; Xu
 481 et al., 2024), to developing strategies to retain model expressivity and generalization while defending
 482 against adversarial attacks (Tsipras et al., 2019; Zhang et al., 2024).

483

484 **Pruning and low-rank approximation.** Prominent compression approaches include pruning, quanti-
 485 zation, distillation, conditional computing, and efficient architecture development (O’Neill, 2020).
 486 Out of these, pruning remains among the most actively researched compression approaches due to
 487 its versatility (Cheng et al., 2024). Inducing compressibility / sparsity at training time is one of



488 Figure 8: Robustness under compression. SA/RA: Standard/Robust Acc. LW/Glob.: Layerwise vs. global pruning.

486 the easiest way to obtain prunable models (Hohman et al., 2024). Compressibility across different
 487 substructures, a.k.a group sparsity (Li et al., 2020b), allows for structured pruning (e.g. neuron/row,
 488 filter/channel, kernel pruning), which is computationally efficient (Yang et al., 2018), yet leads to
 489 a sharp reduction in network connectivity, threatening performance (Blalock et al., 2020). Lastly,
 490 spectral compressibility relaxes the notion of low-rankness, utilized for approximating large matrices
 491 with appealing theoretical properties (Suzuki et al., 2020; Schotthöfer et al., 2022). While nuclear
 492 norm regularization is not a commonly utilized intervention due to the computational costs involved,
 493 low-rank factorization continues to be a prominent architectural design choice due to its attractive
 494 theoretical and empirical properties (Savostianova et al., 2023).

495 **Compressibility and robustness.** Whereas some research argues that compressibility/sparsity is
 496 beneficial for adversarial robustness (Guo et al., 2018; Balda et al., 2020; Liao et al., 2022), others
 497 indicate the relation is *at best* highly dependent on the degree and type of compressibility, as well
 498 as attack type (Li et al., 2020a; Merkle et al., 2022; Savostianova et al., 2023; Feng et al., 2025).
 499 While a stream of new methods that incorporate adversarial robustness in novel ways to pruning (an
 500 approach sometimes termed *adversarial pruning*), newly emerging systematic benchmarks reveal at
 501 best marginal benefits for such methods compared to weight-based pruning (Lee et al., 2020; Piras
 502 et al., 2025). Whereas some methods demonstrate benefits of adversarial training-aware sparsification
 503 (Gui et al., 2019; Sehwag et al., 2020; Pavlitska et al., 2023), infamous problems adversarial training
 504 poses for standard generalization, transferability, as well as computational feasibility especially for
 505 larger models still plague such methods (Tsipras et al., 2019; Wen et al., 2020; Yang et al., 2024).

506 **Comparing our results to previous research.** Our work addresses a critical gap in the literature:
 507 **paucity of research that establishes a principled, theoretical relationship between structured com-**
 508 **pressibility and adversarial robustness with extensive empirical confirmation.** While doing so, we
 509 find that it produces complementary results to most closely related previous work. For example,
 510 Savostianova et al. (2023) and Feng et al. (2025) highlight the adversarial vulnerability created by
 511 increased condition numbers due to high unstructured sparsity or low-rank training, respectively. Our
 512 results complement and extend their conclusions by providing convergent theoretical results with a
 513 more fine-grained, source-agnostic notion of compressibility, and can naturally incorporate neuron
 514 compressibility/prunability, which the cited work do not address. We also find that our results provide
 515 important evidence for research on *adversarial pruning* (Piras et al., 2025). Indeed, in our Appendix
 516 we investigate two prominent structured adversarial pruning methods (Zhao & Wressnegger, 2023;
 517 Zhong et al., 2023), and demonstrate that such methods *implicitly* conduct operator norm control - in
 518 a way that cannot be simply attributed to adversarial training. Our complementary findings highlight
 519 the design of theoretically informed robust pruning methods as a promising future research direction.

520 6 CONCLUSION AND FUTURE WORK

521 In this paper, we present a unified theoretical and empirical treatment of how structured compressibil-
 522 ity shapes adversarial robustness. Via a novel analysis of neuron-level and spectral compressibility,
 523 we uncover a fundamental mechanism: compression concentrates sensitivity along a small number
 524 of directions in representation space, rendering models more vulnerable—even under adversarial
 525 training and transfer learning. Our norm-based robustness bounds offer interpretable decompositions
 526 that predict both standard and universal adversarial vulnerability, and shed light on the trade-offs
 527 between efficiency and safety in modern neural networks. Empirically, we validate these insights
 528 across datasets, architectures, and training regimes, showing how compressibility determines adver-
 529 sarial susceptibility in various learning contexts. Inspired by our bounds, we outline simple, targeted
 530 strategies that can mitigate these vulnerabilities.

531 Our work provides a novel insight into the relationship between structured compressibility and
 532 adversarial vulnerability. A limitation is our theory’s reliance on global Lipschitz constants to
 533 characterize network performance: future work should focus on providing a unified view that
 534 incorporates both structural/global weaknesses, localization of sensitivity in the input space, **as well**
 535 **as incorporating novel Lipschitz estimation methods for tighter bounds.** Extending our work to
 536 incorporate other types of compression (e.g. layer, attention head, or semi-structured pruning) and
 537 distribution shifts (e.g. other ℓ_p attacks, spurious correlations, label noise) are other important future
 538 directions. Moreover, while the simple interventions suggested by our theory provide cost-effective
 539 improvements to the compressibility-robustness trade-off, these insights should be combined with
 alternative, novel compression methods to improve the frontiers of robust compression.

540 REFERENCES

542 Alireza Abdollahpoorrostam, Mahed Abroshan, and Seyed-Mohsen Moosavi-Dezfooli. SuperDeep-
 543 Fool: A new fast and accurate minimal adversarial attack. In *Advances in Neural Information
 544 Processing Systems*, 2024.

545 Arash Amini, Michael Unser, and Farokh Marvasti. Compressibility of Deterministic and Random
 546 Infinite Sequences. *IEEE Transactions on Signal Processing*, 59(11):5193–5201, 2011.

547 Maksym Andriushchenko, Francesco Croce, Nicolas Flammarion, and Matthias Hein. Square Attack:
 548 A Query-Efficient Black-Box Adversarial Attack via Random Search. In *European Conference on
 549 Computer Vision*, 2020.

550 Sanjeev Arora, Rong Ge, Behnam Neyshabur, and Yi Zhang. Stronger generalization bounds for
 551 deep nets via a compression approach. In *International Conference on Machine Learning*, 2018.

552 Emilio Balda, Niklas Koep, Arash Behboodi, and Rudolf Mathar. Adversarial Risk Bounds through
 553 Sparsity based Compression. In *International Conference on Artificial Intelligence and Statistics*,
 554 2020.

555 Melih Barsbey, Milad Sefidgaran, Murat A. Erdogdu, Gaël Richard, and Umut Şimşekli. Heavy
 556 Tails in SGD and Compressibility of Overparametrized Neural Networks. In *Advances in Neural
 557 Information Processing Systems*, 2021.

558 Davis Blalock, Jose Javier Gonzalez Ortiz, Jonathan Frankle, and John Guttag. What is the State of
 559 Neural Network Pruning? *arXiv:2003.03033*, 2020.

560 Sébastien Bubeck, Yuanzhi Li, and Dheeraj Nagaraj. A law of robustness for two-layers neural
 561 networks. *arXiv:2009.14444*, 2020.

562 Hongrong Cheng, Miao Zhang, and Javen Qinfeng Shi. A Survey on Deep Neural Network Pruning:
 563 Taxonomy, Comparison, Analysis, and Recommendations. *IEEE Transactions on Pattern Analysis
 564 and Machine Intelligence*, 46(12):10558–10578, 2024.

565 Moustapha Cisse, Piotr Bojanowski, Edouard Grave, Yann Dauphin, and Nicolas Usunier. Parseval
 566 networks: Improving robustness to adversarial examples. In *International Conference on Machine
 567 Learning*, 2017.

568 Francesco Croce and Matthias Hein. Reliable evaluation of adversarial robustness with an ensemble
 569 of diverse parameter-free attacks. In *International Conference on Machine Learning*, 2020.

570 Jia Deng, Wei Dong, Richard Socher, Li-Jia Li, Kai Li, and Li Fei-Fei. ImageNet: A large-
 571 scale hierarchical image database. In *IEEE/CVF Conference on Computer Vision and Pattern
 572 Recognition*, 2009.

573 Li Deng. The MNIST Database of Handwritten Digit Images for Machine Learning Research. *IEEE
 574 Signal Processing Magazine*, 29(6):141–142, 2012.

575 Enmao Diao, Ganghua Wang, Jiawei Zhang, Yuhong Yang, Jie Ding, and Vahid Tarokh. Pruning
 576 Deep Neural Networks from a Sparsity Perspective. In *International Conference on Learning
 577 Representations*, 2023.

578 Alexey Dosovitskiy, Lucas Beyer, Alexander Kolesnikov, Dirk Weissenborn, Xiaohua Zhai, Thomas
 579 Unterthiner, Mostafa Dehghani, Matthias Minderer, Georg Heigold, Sylvain Gelly, Jakob Uszkoreit,
 580 and Neil Houlsby. An Image is Worth 16x16 Words: Transformers for Image Recognition at Scale.
 581 In *International Conference on Learning Representations*, 2021.

582 Yangqi Feng, Shing-Ho J Lin, Baoyuan Gao, and Xian Wei. Lipschitz constant meets condition
 583 number: Learning robust and compact deep neural networks. *arXiv:2503.20454*, 2025.

584 A. Frank. Some Polynomial Algorithms for Certain Graphs and Hypergraphs. *Utilitas Mathematica*,
 585 1976.

586 Ian Goodfellow, Jonathon Shlens, and Christian Szegedy. Explaining and Harnessing Adversarial
 587 Examples. In *International Conference on Learning Representations*, 2015.

594 Rémi Gribonval, Volkan Cevher, and Mike E. Davies. Compressible Distributions for High-
 595 Dimensional Statistics. *IEEE Transactions on Information Theory*, (8), 2012.

596

597 Ekaterina Grishina, Mikhail Gorbunov, and Maxim Rakhuba. Tight and Efficient Upper Bound
 598 on Spectral Norm of Convolutional Layers. In *European Conference on Computer Vision*, 2025.

599

600 Shupeng Gui, Haotao N Wang, Haichuan Yang, Chen Yu, Zhangyang Wang, and Ji Liu. Model
 601 Compression with Adversarial Robustness: A Unified Optimization Framework. In *Advances in*
 602 *Neural Information Processing Systems*, 2019.

603

604 Yiwen Guo, Chao Zhang, Changshui Zhang, and Yurong Chen. Sparse DNNs with Improved
 605 Adversarial Robustness. In *Advances in Neural Information Processing Systems*, 2018.

606

607 Kaiming He, Xiangyu Zhang, Shaoqing Ren, and Jian Sun. Deep residual learning for image
 608 recognition. In *IEEE/CVF Conference on Computer Vision and Pattern Recognition*, pp. 770–778,
 609 2016.

610

611 Fred Hohman, Mary Beth Kery, Donghao Ren, and Dominik Moritz. Model Compression in Practice:
 612 Lessons Learned from Practitioners Creating On-device Machine Learning Experiences. In *CHI*
 613 *Conference on Human Factors in Computing Systems*, 2024.

614

615 Rasheed Hussain and SherAli Zeadally. Autonomous Cars: Research Results, Issues, and Future
 616 Challenges. *IEEE Communications Surveys & Tutorials*, 21(2):1275–1313, 2019.

617

618 Gabriel Ilharco, Mitchell Wortsman, Ross Wightman, Cade Gordon, Nicholas Carlini, Rohan Taori,
 619 Achal Dave, Vaishaal Shankar, Hongseok Namkoong, John Miller, Hannaneh Hajishirzi, Ali
 620 Farhadi, and Ludwig Schmidt. OpenCLIP, 2021. URL <https://doi.org/10.5281/zenodo.5143773>.

621

622 Andrew Ilyas, Logan Engstrom, Anish Athalye, and Jessy Lin. Black-box Adversarial Attacks with
 623 Limited Queries and Information. In *International Conference on Machine Learning*, 2018.

624

625 Andrew Ilyas, Logan Engstrom, Shibani Santurkar, Brandon Tran, Dimitris Tsipras, and Aleksander
 626 Ma. Adversarial Examples are not Bugs, they are Features. In *Advances in Neural Information*
 627 *Processing Systems*, 2019.

628

629 Alex Krizhevsky and Geoffrey Hinton. Learning multiple layers of features from tiny images.
 630 Technical report, University of Toronto, 2009. URL <https://www.cs.toronto.edu/~kriz/learning-features-2009-TR.pdf>.

631

632 Jaeho Lee, Sejun Park, Sangwoo Mo, Sungsoo Ahn, and Jinwoo Shin. Layer-adaptive Sparsity for
 633 the Magnitude-based Pruning. In *International Conference on Learning Representations*, 2020.

634

635 Fuwei Li, Lifeng Lai, and Shuguang Cui. On the Adversarial Robustness of Feature Selection Using
 636 LASSO. In *International Workshop on Machine Learning for Signal Processing*, 2020a.

637

638 Yawei Li, Shuhang Gu, Christoph Mayer, Luc Van Gool, and Radu Timofte. Group Sparsity: The
 639 Hinge Between Filter Pruning and Decomposition for Network Compression. In *IEEE/CVF*
 640 *Conference on Computer Vision and Pattern Recognition*, 2020b.

641

642 Ningyi Liao, Shufan Wang, Liyao Xiang, Nanyang Ye, Shuo Shao, and Pengzhi Chu. Achieving
 643 adversarial robustness via sparsity. *Machine Learning*, 111(2):685–711, February 2022.

644

645 Ze Liu, Yutong Lin, Yue Cao, Han Hu, Yixuan Wei, Zheng Zhang, Stephen Lin, and Baining Guo.
 646 Swin Transformer: Hierarchical Vision Transformer using Shifted Windows. In *International*
 647 *Conference on Computer Vision*, 2021.

648

649 Aleksander Madry, Aleksandar Makelov, Ludwig Schmidt, Dimitris Tsipras, and Adrian Vladu.
 650 Towards Deep Learning Models Resistant to Adversarial Attacks. In *International Conference on*
 651 *Learning Representations*, 2018.

652

653 TorchVision maintainers and contributors. Torchvision: Pytorch’s computer vision library. <https://github.com/pytorch/vision>, 2016.

648 Jasmita Malik, Raja Muthalagu, and Pranav M. Pawar. A Systematic Review of Adversarial Machine
 649 Learning Attacks, Defensive Controls, and Technologies. *IEEE Access*, 12:99382–99421, 2024.
 650

651 Florian Merkle, Maximilian Samsinger, and Pascal Schöttle. Pruning in the Face of Adversaries. In
 652 *Image Analysis and Processing*, 2022.

653 Takeru Miyato, Toshiki Kataoka, Masanori Koyama, and Yuichi Yoshida. Spectral Normalization
 654 for Generative Adversarial Networks. In *International Conference on Learning Representations*,
 655 2018.

656 Seyed-Mohsen Moosavi-Dezfooli, Alhussein Fawzi, and Pascal Frossard. DeepFool: A Simple and
 657 Accurate Method to Fool Deep Neural Networks. In *IEEE/CVF Conference on Computer Vision*
 658 and *Pattern Recognition*, 2016.

659 Seyed-Mohsen Moosavi-Dezfooli, Alhussein Fawzi, Omar Fawzi, and Pascal Frossard. Universal
 660 adversarial perturbations. In *IEEE/CVF Conference on Computer Vision and Pattern Recognition*,
 661 2017.

662 Ramchandran Muthukumar and Jeremias Sulam. Adversarial Robustness of Sparse Local Lipschitz
 663 Predictors. *SIAM Journal on Mathematics of Data Science*, 5(4):920–948, 2023.

664 Laura F Nern, Harsh Raj, Maurice André Georgi, and Yash Sharma. On transfer of adversarial
 665 robustness from pretraining to downstream tasks. In *Advances in Neural Information Processing*
 666 *Systems*, 2023.

667 Yuval Netzer, Tao Wang, Adam Coates, Alessandro Bissacco, Bo Wu, and Andrew Y Ng. Reading
 668 digits in natural images with unsupervised feature learning. In *NIPS Workshop on Deep*
 669 *Learning and Unsupervised Feature Learning*, 2011. URL <http://ufldl.stanford.edu/housenumbers/>.

670 Maria-Irina Nicolae, Mathieu Sinn, Minh Tran, Beat Buesser, Anish Rawat, Martin Wistuba, Valerio
 671 Zantedeschi, Nathalie Baracaldo, Heiko Ludwig, Ian Molloy, and Ben Edwards. Adversarial
 672 robustness toolbox v1.0.0. *arXiv:1807.01069*, 2018.

673 James O'Neill. An Overview of Neural Network Compression. *arXiv:2006.03669*, 2020.

674 Guillermo Ortiz-Jimenez, Apostolos Modas, Seyed-Mohsen Moosavi-Dezfooli, and Pascal Frossard.
 675 Optimism in the Face of Adversity: Understanding and Improving Deep Learning Through
 676 Adversarial Robustness. *Proceedings of the IEEE*, 109(5):635–659, 2021.

677 Adam Paszke, Sam Gross, Francisco Massa, Adam Lerer, James Bradbury, Gregory Chanan, Trevor
 678 Killeen, Zeming Lin, Natalia Gimelshein, Luca Antiga, Alban Desmaison, Andreas Köpf, Edward
 679 Yang, Zach DeVito, Martin Raison, Alykhan Tejani, Sasank Chilamkurthy, Benoit Steiner, Lu Fang,
 680 Junjie Bai, and Soumith Chintala. PyTorch: An Imperative Style, High-Performance Deep Learning
 681 Library. *arXiv:1912.01703*, 2019.

682 Svetlana Pavlitska, Hannes Grolig, and J. Marius Zollner. Relationship between Model Compression
 683 and Adversarial Robustness: A Review of Current Evidence. In *IEEE Symposium Series on*
 684 *Computational Intelligence*, 2023.

685 Giorgio Piras, Maura Pintor, Ambra Demontis, Battista Biggio, Giorgio Giacinto, and Fabio Roli.
 686 Adversarial pruning: A survey and benchmark of pruning methods for adversarial robustness.
 687 *Pattern Recognition*, 168:111788, 2025.

688 Alec Radford, Jong Wook Kim, Chris Hallacy, Aditya Ramesh, Gabriel Goh, Sandhini Agarwal,
 689 Girish Sastry, Amanda Askell, Pamela Mishkin, Jack Clark, Gretchen Krueger, and Ilya Sutskever.
 690 Learning Transferable Visual Models From Natural Language Supervision. In *International*
 691 *Conference on Machine Learning*, 2021.

692 Pranav Rajpurkar, Emma Chen, Oishi Banerjee, and Eric J. Topol. AI in health and medicine. *Nature*
 693 *Medicine*, 28:31–38, 2022.

702 Antonio Ribeiro, Dave Zachariah, Francis Bach, and Thomas Schön. Regularization properties of
 703 adversarially-trained linear regression. In *Advances in Neural Information Processing Systems*,
 704 2023.

705 Dayana Savostianova, Emanuele Zangrando, Gianluca Ceruti, and Francesco Tudisco. Robust
 706 low-rank training via approximate orthonormal constraints. In *Advances in Neural Information
 707 Processing Systems*, 2023.

708 Kevin Scaman and Aladin Virmaux. Lipschitz regularity of deep neural networks: Analysis and
 709 efficient estimation. In *Advances in Neural Information Processing Systems*, 2018.

710 Steffen Schotthöfer, Emanuele Zangrando, Jonas Kusch, Gianluca Ceruti, and Francesco Tudisco.
 711 Low-rank lottery tickets: Finding efficient low-rank neural networks via matrix differential equa-
 712 tions. In *Advances in Neural Information Processing Systems*, 2022.

713 Vikash Sehwag, Shiqi Wang, Prateek Mittal, and Suman Jana. Hydra: Pruning adversarially robust
 714 neural networks. In *Advances in Neural Information Processing Systems*, 2020.

715 Karen Simonyan and Andrew Zisserman. Very deep convolutional networks for large-scale image
 716 recognition. *arXiv:1409.1556*, 2014.

717 Taiji Suzuki, Hiroshi Abe, Tomoya Murata, Shingo Horiuchi, Kotaro Ito, Tokuma Wachi, So Hirai,
 718 Masatoshi Yukishima, and Tomoaki Nishimura. Spectral Pruning: Compressing Deep Neural
 719 Networks via Spectral Analysis and its Generalization Error. In *International Joint Conference on
 720 Artificial Intelligence*, 2020.

721 Christian Szegedy, Wojciech Zaremba, Ilya Sutskever, Joan Bruna, Dumitru Erhan, Ian Goodfellow,
 722 and Rob Fergus. Intriguing properties of neural networks. *arXiv:1312.6199*, 2014.

723 Dimitris Tsipras, Shibani Santurkar, Logan Engstrom, Alexander Turner, and Aleksander Madry.
 724 Robustness May Be at Odds with Accuracy. *arXiv:1805.12152*, 2019.

725 Yijun Wan, Melih Barsbey, Abdellatif Zaidi, and Umut Simsekli. Implicit Compressibility of
 726 Overparametrized Neural Networks Trained with Heavy-Tailed SGD. In *International Conference on
 727 Machine Learning*, 2024.

728 Yuxin Wen, Shuai Li, and Kui Jia. Towards understanding the regularization of adversarial robustness
 729 on neural networks. In *International Conference on Machine Learning*, 2020.

730 Thomas Wolf, Lysandre Debut, Victor Sanh, Julien Chaumond, Clement Delangue, Anthony Moi,
 731 Pierrick Cistac, Tim Rault, Rémi Louf, Morgan Funtowicz, Joe Davison, Sam Shleifer, Patrick von
 732 Platen, Clara Ma, Yacine Jernite, Julien Plu, Canwen Xu, Teven Le Scao, Sylvain Gugger, Mariama
 733 Drame, Quentin Lhoest, and Alexander M. Rush. HuggingFace’s Transformers: State-of-the-art
 734 Natural Language Processing. *arXiv:1910.03771*, 2020.

735 Tianlong Xu, Chen Wang, Gaoyang Liu, Yang Yang, Kai Peng, and Wei Liu. United We Stand,
 736 Divided We Fall: Fingerprinting Deep Neural Networks via Adversarial Trajectories. *Advances in
 737 Neural Information Processing Systems*, 2024.

738 Keiichiro Yamamura, Haruiki Sato, Nariaki Tateiwa, Nozomi Hata, Toru Mitsutake, Issa Oe, Hiroki
 739 Ishikura, and Katsuki Fujisawa. Diversified Adversarial Attacks based on Conjugate Gradient
 740 Method. In *International Conference on Machine Learning*, 2022.

741 Carl Yang, Aydin Buluç, and John D. Owens. Design Principles for Sparse Matrix Multiplication on
 742 the GPU. In *International Conference on Parallel and Distributed Computing*, 2018.

743 Sheng Yang, Jacob A. Zavatone-Veth, and Cengiz Pehlevan. Spectral regularization for adversarially-
 744 robust representation learning. *arXiv:2405.17181*, 2024.

745 Peter Young, Alice Lai, Micah Hodosh, and Julia Hockenmaier. From image descriptions to visual
 746 denotations: New similarity metrics for semantic inference over event descriptions. *Transactions
 747 of the Association for Computational Linguistics*, 2:67–78, 2014.

748 Sergey Zagoruyko and Nikos Komodakis. Wide residual networks. *arXiv:1605.07146*, 2016.

756 Kaibo Zhang, Yunjuan Wang, and Raman Arora. Stability and Generalization of Adversarial Training
757 for Shallow Neural Networks with Smooth Activation. *Advances in Neural Information Processing*
758 *Systems*, 2024.

759

760 Qi Zhao and Christian Wressnegger. Holistic Adversarially Robust Pruning. In *International*
761 *Conference on Learning Representations*, 2023.

762

763 Shaochen (Henry) Zhong, Zaichuan You, Jiamu Zhang, Sebastian Zhao, Zachary LeClaire, Zirui
764 Liu, Daochen Zha, Vipin Chaudhary, Shuai Xu, and Xia Hu. One Less Reason for Filter Pruning:
765 Gaining Free Adversarial Robustness with Structured Grouped Kernel Pruning. In *Advances in*
766 *Neural Information Processing Systems*, 2023.

767

768 Monty-Maximilian Zühlke and Daniel Kudenko. Adversarial Robustness of Neural Networks from
769 the Perspective of Lipschitz Calculus: A Survey. *ACM Comput. Surv.*, 57(6):142:1–142:41, 2025.

770

771

772

773

774

775

776

777

778

779

780

781

782

783

784

785

786

787

788

789

790

791

792

793

794

795

796

797

798

799

800

801

802

803

804

805

806

807

808

809

810
 811
 812
 813
 814
 815
 816
 817
 818 **On the Interaction of**
 819 **Compressibility and Adversarial Robustness**
 820 **-Appendix-**
 821
 822
 823
 824
 825
 826
 827
 828

829 **Contents**
 830
 831
 832
 833
 834
 835
 836

837 A Proofs	2
838	
839 B Additional Technical Results and Analyses	7
840 B.1 (q, k, ϵ) -compressibility vs. other notions of approximate sparsity	7
841 B.2 Lower bounds on operator norms	8
842 B.3 Relationships between operator norms	9
843 B.4 Empirical analyses of the robustness bound and related quantities	10
844 B.5 Approximating the interlayer alignment terms	11
845	
846 C Details of the Experimental Settings	12
847 C.1 Datasets	12
848 C.2 Models	12
849 C.3 Standard and Adversarial Training	13
850 C.4 Implementation and Hardware	13
851	
852 D Additional Empirical Results	13
853 D.1 Experiments with other datasets and architectures	13
854 D.2 Group sparsity regularization	13
855 D.3 Adversarial training results for spectral compressibility	14
856 D.4 Compressibility through inductive bias	14
857 D.5 Unstructured compressibility	14
858 D.6 Results with alternative norms, budgets, and attacks	14
859 D.7 Fine-tuning results with transformers	15
860 D.8 Results with post-pruning fine-tuning	15
861 D.9 Exploitation of vulnerable latent directions	16
862 D.9.1 How do such directions get exploited in practice?	17
863 D.9.2 How do white box and black box attacks find these directions?	18
864 D.9.3 Interlayer alignment	18
865 D.10 Comparison with adversarial pruning literature	20
866 D.11 Further experiments with UAEs	20
867	
868	
869	
870	
871	
872	
873	

864 **A PROOFS**
 865

866 We start with a number of auxiliary results that are used in the theorems and corollary presented in
 867 Section 3.

868 **Lemma A.1.** *For any strictly (q, k, ϵ) -compressible vector θ and for all $q \geq 1$, $\|\theta^{(k)}\|_q = (1 -$
 869 $\epsilon^q)^{1/q} \|\theta\|_q$.*

870 *Proof.* $\|\theta - \theta^{(k)}\|_q^q = \epsilon^q \|\theta\|_q^q$ follows from the definition of compressibility. Adding $\|\theta^{(k)}\|_q^q$ to both
 871 sides leads to $\|\theta\|_q^q = \epsilon^q \|\theta\|_q^q + \|\theta^{(k)}\|_q^q$, with LHS due to elements of x and $\theta - \theta^{(k)}$ populating
 872 disjoint sets of coordinates. Result follows with simple algebraic manipulation. \square

873 Note that for the results in this section, we use $\theta^{(k)}$ and θ_k equivalently to denote a vector that
 874 includes only the k dominant terms.

875 **Lemma A.2.** *For $p^* < q$, given the $(2, k, \epsilon)$ -compressible vector $\theta \in \mathbb{R}^d$, we have:*

$$876 \|\theta\|_{p^*} \leq k^{\frac{1}{p^*} - \frac{1}{q}} \|\theta^{(k)}\|_q + d^{\frac{1}{p^*} - \frac{1}{q}} \epsilon \|\theta\|_q. \quad (10)$$

877 *Proof.* We start by applying Minkowski's inequality to $\|\theta\|_{p^*}$:

$$878 \|\theta\|_{p^*} \leq \|\theta^{(k)}\|_{p^*} + \|\theta - \theta^{(k)}\|_{p^*}. \quad (11)$$

879 We now bound the terms on RHS separately. For the first term, since $p^* < q$ by Hölder's inequality
 880 for k -sparse vectors we have

$$881 \|\theta^{(k)}\|_{p^*} \leq k^{\frac{1}{p^*} - \frac{1}{q}} \|\theta^{(k)}\|_q.$$

882 For the next term, we can write

$$883 \|\theta - \theta^{(k)}\|_{p^*} \leq d^{\frac{1}{p^*} - \frac{1}{q}} \|\theta - \theta^{(k)}\|_q \leq d^{\frac{1}{p^*} - \frac{1}{q}} \epsilon \|\theta\|_q,$$

884 with the left inequality due to Hölder's inequality, and the right due to $\theta^{(k)}$'s (q, k, ϵ) compressibility.
 885 Combining the expressions for both terms, we have

$$886 \|\theta\|_{p^*} \leq k^{\frac{1}{p^*} - \frac{1}{q}} \|\theta^{(k)}\|_q + d^{\frac{1}{p^*} - \frac{1}{q}} \epsilon \|\theta\|_q. \quad (12)$$

887 \square

888 **Proposition A.3.** *Given a linear binary classifier and binary cross-entropy loss function, we have
 889 the following bound:*

$$890 F_p^{\text{adv}}(\theta; \delta) \leq F(\theta; \delta) + \delta \|\theta\|_{p^*} \quad (13)$$

891 *Proof of Proposition A.3.* For binary cross-entropy loss we have:

$$892 f^{\text{adv}}(\mathbf{x}, \theta; \delta) = \log(1 + \exp(-y(\mathbf{x}^\top \theta) + \delta \|\theta\|_{p^*})).$$

893 We observe that $f^{\text{adv}}(\mathbf{x}, \theta; \delta) \leq f(\mathbf{x}, \theta; \delta) + \delta \|\theta\|_{p^*}$ since

$$894 \begin{aligned} f^{\text{adv}}(\mathbf{x}, \theta; \delta) &= \log(1 + \exp(-y(\mathbf{x}^\top \theta) + \delta \|\theta\|_{p^*})) \\ 895 &= \log(1 + \exp(-y(\mathbf{x}^\top \theta))) + \log\left(\frac{1 + \exp(-y(\mathbf{x}^\top \theta) + \delta \|\theta\|_{p^*})}{1 + \exp(-y(\mathbf{x}^\top \theta))}\right) \\ 896 &= f(\mathbf{x}, \theta; \delta) + \log\left(1 + (\exp(\delta \|\theta\|_{p^*}) - 1) \frac{\exp(-y(\mathbf{x}^\top \theta))}{1 + \exp(-y(\mathbf{x}^\top \theta))}\right) \\ 897 &\leq f(\mathbf{x}, \theta; \delta) + \delta \|\theta\|_{p^*}, \end{aligned}$$

898 with the last inequality due to the fact that $\frac{\exp(-y(\mathbf{x}^\top \theta))}{1 + \exp(-y(\mathbf{x}^\top \theta))} < 1$. Taking the expectation of the
 899 expression gives:

$$900 F^{\text{adv}}(\theta; \delta) \leq F(\theta; \delta) + \delta \|\theta\|_{p^*}$$

901 \square

918 **Main results.** We now present the proofs for Theorem 3.1 and 3.2 and Corollary 3.3.
919

920 *Proof of Theorem 3.1.* For brevity we will omit ν as a subscript, such that $\epsilon = \epsilon_\nu, k = k_\nu, \beta = \beta_\nu$.
921

922 For **(a)**, we assume ν is in a descending order w.l.o.g., and $\hat{\nu}$ is the corresponding vector of ℓ_2 norms
923 for each row. We note that

$$924 \quad 925 \quad 926 \quad \|\nu^{(k)}\|_1 = \sum_{i=1}^k \nu_i \geq k\nu_k \quad (14)$$

$$927 \quad 928 \quad 929 \quad \geq k(1 - \beta)\nu_1 \quad (15)$$

$$930 \quad 931 \quad 932 \quad (1 - \epsilon)\|\nu\|_1 \geq k(1 - \beta)\nu_1 \quad (16)$$

$$933 \quad 934 \quad 935 \quad \frac{(1 - \epsilon)}{(1 - \beta)} \frac{1}{k} \|\nu\|_1 \geq \nu_1 \quad (17)$$

$$936 \quad 937 \quad 938 \quad \frac{(1 - \epsilon)}{(1 - \beta)} \frac{1}{k} \|\nu\|_1 \geq \|\mathbf{W}\|_\infty \quad (18)$$

939 with (14) being the smallest magnitude element in $\nu^{(k)}$, (15) due to the definition of slack variable
940 β , and (16) due to Lemma A.1, and (18) due to the fact that $\|\mathbf{W}\|_\infty = \nu_1$, as ν is assumed to be
941 magnitude-ordered. We then move on to characterizing $\|\nu\|_1$. Notice that

$$942 \quad 943 \quad 944 \quad \|\nu\|_1 = \sum_{i=1}^h \nu_i \leq \sum_{i=1}^h \sqrt{h}\hat{\nu}_i \quad (19)$$

$$945 \quad 946 \quad 947 \quad \leq \sqrt{h}\|\hat{\nu}\|_1 \quad (20)$$

$$948 \quad 949 \quad 950 \quad \leq \sqrt{h} \left(\sqrt{k_r} \|\hat{\nu}^{(k_r)}\|_2 + \sqrt{h} \|\hat{\nu}\|_2 \right) \quad (21)$$

$$951 \quad 952 \quad 953 \quad \leq \left(\sqrt{hk_r} + \sqrt{h}\epsilon_r \right) \|\hat{\nu}\|_2 \quad (22)$$

$$954 \quad 955 \quad 956 \quad \leq \left(\sqrt{hk_r} + \sqrt{h}\epsilon_r \right) \|\mathbf{W}\|_F \quad (23)$$

957 Note that (19) is due to standard norm inequality between ℓ_1 and ℓ_2 rows, (21) is due to Lemma A.2,
958 and (23) is due to ℓ_2 norm of the vector of row ℓ_2 rows equals the Frobenius norm. Plugging (23)
959 back into (18) gives the desired result.

960 For **(b)** the proof follows similarly through steps (14)-(17) by replacing ν with σ . After that, we
961 continue with

$$962 \quad 963 \quad 964 \quad \frac{(1 - \epsilon)}{(1 - \beta)} \frac{1}{k} \|\sigma\|_1 \geq \sigma_1 \quad (24)$$

$$965 \quad 966 \quad 967 \quad \frac{(1 - \epsilon)}{(1 - \beta)} \frac{1}{k} \|\sigma\|_1 \geq \|\mathbf{W}\|_2 \quad (25)$$

$$968 \quad 969 \quad 970 \quad \frac{(1 - \epsilon)}{(1 - \beta)} \frac{\sqrt{h}}{k} \|\sigma\|_2 \geq \|\mathbf{W}\|_2 \quad (26)$$

$$971 \quad 972 \quad 973 \quad \frac{(1 - \epsilon)}{(1 - \beta)} \frac{\sqrt{h}}{k} \|\mathbf{W}\|_F \geq \|\mathbf{W}\|_2 \quad (27)$$

974 with (25) due to $\|\mathbf{W}\|_2 = \sigma_1$, (26) due to standard norm inequality between ℓ_1 and ℓ_2 norms, and
975 (27) due to the fact that ℓ_2 norm of singular values equals Frobenius norm, i.e. $\|\mathbf{W}\|_F = \|\sigma\|_2$. \square

976 *Proof of Theorem 3.2.* Proofs for both conditions rely on an additive decomposition of the layer
977 matrices \mathbf{W}^l into dominant/leading terms vs. remainder terms, i.e. $\mathbf{W}^l = \mathbf{W}_k^l + \mathbf{W}_r^l$. In structured
978 compressibility this takes the form of \mathbf{W}_k^l and \mathbf{W}_r^l including k leading (largest ℓ_1 norm) rows and
979 $h - k$ remaining rows, respectively, with the rest of the rows set to $\mathbf{0}$ in both cases. In spectral
980 compressibility, this takes the form of $\mathbf{W}_k^l + \mathbf{W}_r^l = \mathbf{U}_k^l \Sigma_k^l (\mathbf{V}_k^l)^\top + \mathbf{U}_r^l \Sigma_r^l (\mathbf{V}_r^l)^\top$, where the
981 remaining $h - k$ vs. leading k singular values are set to 0 respectively.

Let \mathbf{z}^l denote the post-activation representations of the network after layer $l \in [\lambda]$. The Jacobian of the network output \mathbf{z}^λ with respect to the input \mathbf{x} is given by:

$$\mathbf{J}_\Phi(\mathbf{x}) = \mathbf{D}^\lambda(\mathbf{x}) \mathbf{W}^\lambda \mathbf{D}^{\lambda-1}(\mathbf{x}) \mathbf{W}^{\lambda-1} \mathbf{D}^{\lambda-2}(\mathbf{x}) \dots \mathbf{D}^1(\mathbf{x}) \mathbf{W}^1, \quad (28)$$

where $\mathbf{D}^l(\mathbf{x})$ is the diagonal binary matrix corresponding to the ReLU activation after layer l , i.e., $(\mathbf{D}^l)_{ii} = \mathbb{I}[(\mathbf{z}^l)_i > 0]$, with \mathbf{z}^l being the pre-activation representation at layer l for input \mathbf{x} .

Letting L_Φ^p denote the p -norm Lipschitz constant of the encoder in the input domain, it can be computed as the maximum $p \rightarrow p$ operator norm of the Jacobian over the input space \mathcal{X} :

$$L_\Phi^p = \sup_{\mathbf{x} \in \mathcal{X}} \|\mathbf{J}_\Phi(\mathbf{x})\|_p = \sup_{\mathbf{x} \in \mathcal{X}} \|\mathbf{D}^\lambda(\mathbf{x}) \mathbf{W}^\lambda \mathbf{D}^{\lambda-1}(\mathbf{x}) \mathbf{W}^{\lambda-1} \dots \mathbf{D}^1(\mathbf{x}) \mathbf{W}^1\|_p. \quad (29)$$

For brevity, we use the following notation:

$$\mathbf{P}(\mathbf{D}) := \mathbf{D}^\lambda(\mathbf{x}) \mathbf{W}^\lambda \mathbf{D}^{\lambda-1}(\mathbf{x}) \mathbf{W}^{\lambda-1} \dots \mathbf{D}^1(\mathbf{x}) \mathbf{W}^1. \quad (30)$$

Note that the optimization over \mathcal{X} can be replaced with the optimization over all binary activation matrices $\mathbf{D}^l \in \mathcal{D}$ for each layer whenever convenient. We replace the notation $\mathbf{D}^l(\mathbf{x})$ with \mathbf{D}^l when doing so.

Note that in this proof, for increased precision and brevity we introduce the following notation for the interlayer alignment terms:

$$A_{p,l}^* := \max_{\mathbf{D} \in \mathcal{D}} A_{p,l} \quad (31)$$

where $A_{p,l}$ stands for the inner RHS term optimized over in (6) and (7).

(a) Row/neuron compressibility We aim to bound L_Φ^∞ as:

$$L_\Phi^\infty \leq \max_{\mathbf{D}^1, \dots, \mathbf{D}^\lambda} \|\mathbf{P}(\mathbf{D})\|_\infty. \quad (32)$$

We start by noting that we can upper bound this norm by partitioning the inside terms based on the submultiplicative property:

$$\|\mathbf{P}(\mathbf{D})\|_\infty \leq \|\mathbf{D}^\lambda \mathbf{W}^\lambda \mathbf{D}^{\lambda-1} \mathbf{W}^{\lambda-1} \dots \mathbf{D}^1 \mathbf{W}^1\|_\infty \quad (33)$$

$$\leq \|\mathbf{W}^\lambda \mathbf{D}^{\lambda-1} \mathbf{W}^{\lambda-1}\|_\infty \|\mathbf{D}^{\lambda-2}\|_\infty \|\mathbf{W}^{\lambda-2}\|_\infty \dots \|\mathbf{W}^{l+1} \mathbf{D}^l \mathbf{W}^l\|_\infty \dots \|\mathbf{D}^1\|_\infty \|\mathbf{W}^1\|_\infty \quad (34)$$

Note that any such parsing is valid as long as a layer does not appear in two interlayer terms at once. Given a valid parsing set $S \subseteq \{1, 2, \dots, \lambda-1\}$, we have the interlayer alignment terms for $l \in S$, i.e. $\|\mathbf{W}^{l+1} \mathbf{D}^l \mathbf{W}^l\|_\infty$ and standalone terms for all remaining layers $\{l \mid l \notin S, l+1 \notin S\}$: $\|\mathbf{W}^l\|_\infty$. We denote all such valid parsing layer subsets with \mathcal{S} , where S does not include any consecutive indices for any $S \in \mathcal{S}$. We will first prove the bound for any valid parsing set, and then define the optimal alignment parsing set that would lead to the tightest bound.

We first analyze a generic alignment term, using the additive decomposition into leading and remainder terms. Remember that for layer l we denote the row ℓ_1 norms with $\boldsymbol{\nu}^l = (\nu_1^l, \dots, \nu_h^l)$, and w.l.o.g. assume that the rows are ordered in descending order according to ν_l . Also note that $\|\mathbf{W}_k^l\|_\infty = \|\mathbf{W}^l\|_\infty = \nu_1^l$.

$$\begin{aligned} \|\mathbf{W}^{l+1} \mathbf{D}^l \mathbf{W}^l\|_\infty &\leq \|\mathbf{W}_k^{l+1} \mathbf{D}^l \mathbf{W}_k^l\|_\infty + \|\mathbf{W}_k^{l+1} \mathbf{D}^l \mathbf{W}_r^l\|_\infty \\ &\quad + \|\mathbf{W}_r^{l+1} \mathbf{D}^l \mathbf{W}_k^l\|_\infty + \|\mathbf{W}_r^{l+1} \mathbf{D}^l \mathbf{W}_r^l\|_\infty \end{aligned} \quad (35)$$

$$\begin{aligned} &\leq \|\mathbf{W}_k^{l+1} \mathbf{D}^l \mathbf{W}_k^l\|_\infty + \|\mathbf{W}_k^{l+1}\|_\infty \|\mathbf{W}_r^l\|_\infty \\ &\quad + \|\mathbf{W}_r^{l+1}\|_\infty \|\mathbf{W}_k^l\|_\infty + \|\mathbf{W}_r^{l+1}\|_\infty \|\mathbf{W}_r^l\|_\infty \end{aligned} \quad (36)$$

$$\begin{aligned} &\leq \|\mathbf{W}^{l+1}\|_\infty \|\mathbf{W}^l\|_\infty \left(\frac{\|\mathbf{W}_k^{l+1} \mathbf{D}^l \mathbf{W}_k^l\|_\infty}{\|\mathbf{W}^{l+1}\|_\infty \|\mathbf{W}^l\|_\infty} + \frac{\nu_{k+1}^l}{\nu_1^l} \right. \\ &\quad \left. + \frac{\nu_{k+1}^{l+1}}{\nu_1^{l+1}} + \frac{\nu_{k+1}^l \nu_{k+1}^{l+1}}{\nu_1^l \nu_1^{l+1}} \right). \end{aligned} \quad (37)$$

$$\leq \|\mathbf{W}^{l+1}\|_\infty \|\mathbf{W}^l\|_\infty \left(\frac{\|\mathbf{W}_k^{l+1} \mathbf{D}^l \mathbf{W}_k^l\|_\infty}{\|\mathbf{W}^{l+1}\|_\infty \|\mathbf{W}^l\|_\infty} + R_\infty(\epsilon) \right). \quad (38)$$

1026 Since the remaining, standalone layer norms also contribute $\|\mathbf{W}^l\|_\infty$, we have
 1027

$$1028 \|\mathbf{P}(\mathbf{D})\|_\infty \leq \prod_{l=1}^{\lambda} \|\mathbf{W}^l\|_\infty \prod_{l \in S} \left(\frac{\|\mathbf{W}_k^{l+1} \mathbf{D}^l \mathbf{W}_k^l\|_\infty}{\|\mathbf{W}^{l+1}\|_\infty \|\mathbf{W}^l\|_\infty} + R_\infty(\epsilon) \right). \quad (39)$$

1031 Bounding the Lipschitz constant accordingly:
 1032

$$1033 L_\Phi^\infty \leq \max_{\mathbf{D}^1, \dots, \mathbf{D}^\lambda} \prod_{l=1}^{\lambda} \|\mathbf{W}^l\|_\infty \prod_{l=1}^{\lambda-1} \left(\frac{\|\mathbf{W}_k^{l+1} \mathbf{D}^l \mathbf{W}_k^l\|_\infty}{\|\mathbf{W}^{l+1}\|_\infty \|\mathbf{W}^l\|_\infty} + R_\infty(\epsilon) \right) \quad (40)$$

$$1036 = \prod_{l=1}^{\lambda} \|\mathbf{W}^l\|_\infty \prod_{l \in S} \left(\max_{\mathbf{D} \in \mathcal{D}} \frac{\|\mathbf{W}_k^{l+1} \mathbf{D} \mathbf{W}_k^l\|_\infty}{\|\mathbf{W}^{l+1}\|_\infty \|\mathbf{W}^l\|_\infty} + R_\infty(\epsilon) \right) \quad (41)$$

$$1039 = \prod_{l=1}^{\lambda} \|\mathbf{W}^l\|_\infty \prod_{l \in S} A_\infty^*(\mathbf{W}^{l+1}, \mathbf{W}^l) + R_\infty(\epsilon). \quad (42)$$

1042 Contributing an alignment term of 1 for $\{l \mid l \notin S, l+1 \notin S\}$ gives the desired result if $S = S_{opt}$,
 1043 which we define below.

1044 Given multiple valid parsing sets are possible whenever $\lambda > 2$, we lastly define the *optimal alignment*
 1045 *parsing set*, S_{opt} .

1046 **Definition A.4** (Optimal Alignment Parsing Set). *The Optimal Alignment Parsing Set S_{opt} is a set in*
 1047 *S that achieves the minimum product of the corresponding maximum alignment factors:*

$$1049 S_{opt} \in \arg \min_{S \in \mathcal{S}} \prod_{l \in S} A_{\infty, l}^*. \quad (43)$$

1050 Note that S_{opt} might not be unique, but $\min_{S \in \mathcal{S}} \prod_{l \in S} A_{\infty, l}^*$ is.
 1051

1052 **Complexity of finding S_{opt} :** Finding $S_{opt} \in \arg \min_{S \in \mathcal{S}} \prod_{l \in S} A_{\infty, l}^*$ is equivalent to finding the
 1053 independent set S in the path graph $G = (V, E)$ with $V = \{1, \dots, L-1\}$ that maximizes $\sum_{l \in S} w_l$,
 1054 where weights $w_l = -\log A_{\infty, l}^*$ (assuming $A_{\infty, l}^* > 0$; we handle $A_{\infty, l}^* = 0$ as a special case yielding
 1055 $\prod_{l \in S_{opt}} A_{\infty, l}^* = 0$). This is the Maximum Weight Independent Set, which can be solved in linear
 1056 time in chordal graphs, of which path graphs are a subfamily (Frank, 1976).

1057 **(b) Spectral compressibility:** We can upper bound L_Φ^2 by considering all possible activation patterns
 1058 (all possible binary diagonal matrices \mathbf{D}^l):
 1059

$$1060 L_\Phi^2 \leq \max_{\mathbf{D}^1, \dots, \mathbf{D}^\lambda} \|\mathbf{P}(\mathbf{D})\|_2 \quad (44)$$

1061 We modify the SVD decomposition for layers as
 1062

$$1063 \mathbf{W}^l = \mathbf{U}^l \sqrt{\Sigma^l} \sqrt{\Sigma^l} (\mathbf{V}^l)^\top \quad (45)$$

$$1064 = \underbrace{\left(\mathbf{U}_k^l \sqrt{\Sigma_k^l} + \mathbf{U}_r^l \sqrt{\Sigma_r^l} \right)}_{\mathbf{A}^l} \underbrace{\left(\sqrt{\Sigma_k^l} (\mathbf{V}_k^l)^\top + \sqrt{\Sigma_r^l} (\mathbf{V}_r^l)^\top \right)}_{\mathbf{B}^l}. \quad (46)$$

1065 Note that we assume untruncated singular vector matrices for \mathbf{W}_k^l and \mathbf{W}_r^l for the equation above to
 1066 be valid. We then decompose the spectral norm using the submultiplicative property:
 1067

$$1068 \|\mathbf{P}(\mathbf{D})\|_2 = \|\mathbf{D}^\lambda \mathbf{W}^\lambda \mathbf{D}^{\lambda-1} \mathbf{W}^{\lambda-1} \mathbf{D}^{\lambda-2} \dots \mathbf{D}^1 \mathbf{W}^1\|_2 \quad (47)$$

$$1069 \leq \|\mathbf{A}^\lambda\|_2 \|\mathbf{B}^\lambda \mathbf{D}^{\lambda-1} \mathbf{A}^{\lambda-1}\|_2 \|\mathbf{B}^{\lambda-1} \mathbf{D}^{\lambda-2} \mathbf{A}^{\lambda-2}\|_2 \dots \|\mathbf{B}^{l+1} \mathbf{D}^l \mathbf{A}^l\|_2 \dots \|\mathbf{B}^2 \mathbf{D}^1 \mathbf{A}^1\|_2 \|\mathbf{B}^1\|_2 \quad (48)$$

1070 We then analyze the central term $\|\mathbf{B}^{l+1} \mathbf{D}^l \mathbf{A}^l\|_2$, and decompose it using the submultiplicative
 1071 and subadditivity properties. Remember that for layer l we denote the singular values with $\sigma^l =$
 1072

1080 $(\sigma_1^l, \dots, \sigma_h^l)$. Also note that $\|\mathbf{W}_k^l\|_2 = \|\mathbf{W}^l\|_2 = \sigma_1^l$.
1081

$$\begin{aligned} 1082 & \|\mathbf{B}^{l+1} \mathbf{D}^l \mathbf{A}^l\|_2 \\ 1083 & \leq \|\sqrt{\Sigma_k^{l+1}} (\mathbf{V}_k^{l+1})^\top \mathbf{D}^l \mathbf{U}_k^l \sqrt{\Sigma_k^l}\|_2 + \|\sqrt{\Sigma_k^{l+1}} (\mathbf{V}_k^{l+1})^\top \mathbf{D}^l \mathbf{U}_r^l \sqrt{\Sigma_r^l}\|_2 \\ 1084 & \quad + \|\sqrt{\Sigma_r^{l+1}} (\mathbf{V}_r^{l+1})^\top \mathbf{D}^l \mathbf{U}_k^l \sqrt{\Sigma_k^l}\|_2 + \|\sqrt{\Sigma_r^{l+1}} (\mathbf{V}_r^{l+1})^\top \mathbf{D}^l \mathbf{U}_r^l \sqrt{\Sigma_r^l}\|_2 \end{aligned} \quad (49)$$

$$\begin{aligned} 1085 & \leq \|\sqrt{\Sigma_k^{l+1}} (\mathbf{V}_k^{l+1})^\top \mathbf{D}^l \mathbf{U}_k^l \sqrt{\Sigma_k^l}\|_2 + \sqrt{\sigma_1^{l+1}} \|(\mathbf{V}_k^{l+1})^\top \mathbf{D}^l \mathbf{U}_r^l\|_2 \sqrt{\sigma_{k+1}^l} \\ 1086 & \quad + \sqrt{\sigma_{k+1}^{l+1}} \|(\mathbf{V}_r^{l+1})^\top \mathbf{D}^l \mathbf{U}_r^l\|_2 \sqrt{\sigma_1^l} + \sqrt{\sigma_{k+1}^{l+1}} \|(\mathbf{V}_r^{l+1})^\top \mathbf{D}^l \mathbf{U}_r^l\|_2 \sqrt{\sigma_{k+1}^l} \end{aligned} \quad (50)$$

$$\begin{aligned} 1087 & \leq \sqrt{\sigma_1^{l+1}} \sqrt{\sigma_1^l} \left(\frac{\|\sqrt{\Sigma_k^{l+1}} (\mathbf{V}_k^{l+1})^\top \mathbf{D}^l \mathbf{U}_k^l \sqrt{\Sigma_k^l}\|_2}{\sqrt{\sigma_1^l \sigma_1^{l+1}}} + \sqrt{\frac{\sigma_{k+1}^{l+1}}{\sigma_1^l}} + \sqrt{\frac{\sigma_{k+1}^{l+1}}{\sigma_1^{l+1}}} + \sqrt{\frac{\sigma_{k+1}^l \sigma_{k+1}^{l+1}}{\sigma_1^l \sigma_1^{l+1}}} \right) \\ 1088 & \quad (51) \\ 1089 & \leq \sqrt{\sigma_1^{l+1}} \sqrt{\sigma_1^l} \left(\frac{\|\sqrt{\Sigma_k^{l+1}} (\mathbf{V}_k^{l+1})^\top \mathbf{D}^l \mathbf{U}_k^l \sqrt{\Sigma_k^l}\|_2}{\sqrt{\sigma_1^l \sigma_1^{l+1}}} + R_2(\epsilon) \right), \end{aligned} \quad (52)$$

1100 where we set all cross-alignment terms other than dominant-dominant interaction to 1. This is made
1101 possible by the fact that they are the multiplication of orthogonal matrices and a ReLU matrix, all
1102 of which have spectral norms upper bounded by 1. Note that for all layers $l \in 1, \dots, \lambda$, $\sqrt{\sigma_1^l}$ will
1103 appear twice in the multiplication, including the first and last layers due to the leading and final terms
1104 in (48), leading to the expression:

$$\begin{aligned} 1105 & \|\mathbf{P}(\mathbf{D})\|_2 \leq \prod_{l=1}^{\lambda} \|\mathbf{W}^l\|_2 \prod_{l=1}^{\lambda-1} \left(\frac{\|\sqrt{\Sigma_k^{l+1}} (\mathbf{V}_k^{l+1})^\top \mathbf{D}^l \mathbf{U}_k^l \sqrt{\Sigma_k^l}\|_2}{\sqrt{\sigma_1^l \sigma_1^{l+1}}} + R_2(\epsilon) \right) \end{aligned} \quad (53)$$

1109 Bounding the Lipschitz constant:

$$1110 L_{\Phi}^2 \leq \max_{\mathbf{D}^1, \dots, \mathbf{D}^{\lambda}} \|\mathbf{P}(\mathbf{D})\|_2 \quad (54)$$

$$\begin{aligned} 1111 & \leq \max_{\mathbf{D}^1, \dots, \mathbf{D}^{\lambda}} \prod_{l=1}^{\lambda} \|\mathbf{W}^l\|_2 \prod_{l=1}^{\lambda-1} \left(\frac{\|\sqrt{\Sigma_k^{l+1}} (\mathbf{V}_k^{l+1})^\top \mathbf{D}^l \mathbf{U}_k^l \sqrt{\Sigma_k^l}\|_2}{\sqrt{\sigma_1^l \sigma_1^{l+1}}} + R_2(\epsilon) \right) \end{aligned} \quad (55)$$

$$\begin{aligned} 1112 & \leq \prod_{l=1}^{\lambda} \|\mathbf{W}^l\|_2 \prod_{l=1}^{\lambda-1} \left(\max_{\mathbf{D} \in \mathcal{D}} \frac{\|\sqrt{\Sigma_k^{l+1}} (\mathbf{V}_k^{l+1})^\top \mathbf{D}^l \mathbf{U}_k^l \sqrt{\Sigma_k^l}\|_2}{\sqrt{\sigma_1^l \sigma_1^{l+1}}} + R_2(\epsilon) \right) \end{aligned} \quad (56)$$

$$\begin{aligned} 1113 & \leq \prod_{l=1}^{\lambda} \|\mathbf{W}^l\|_2 \prod_{l=1}^{\lambda-1} A_2^*(\mathbf{W}_k^{l+1}, \mathbf{W}_k^l), \end{aligned} \quad (57)$$

1123 yielding the desired result. □

1126 *Proof of Corollary 3.3.* Let \mathbf{a} denote the adversarial perturbation on the input \mathbf{x} , where $\|\mathbf{a}\|_p \leq \delta$.
1127 We define the *effective perturbation budget* in ℓ_p norm for the feature encoder Φ_k as $\delta_p^{\Phi_k} :=$
1128 $\max \|\Phi(\mathbf{x}) - \Phi(\mathbf{x} + \mathbf{p})\|_p$. Note that by definition of the Lipschitz constant and by Theorem 3.2, we
1129 have

$$1130 \delta_p^{\Phi} = \max \|\Phi(\mathbf{x}) - \Phi(\mathbf{x} + \mathbf{a})\|_p \leq \|\mathbf{x} - (\mathbf{x} + \mathbf{a})\|_p L_{\Phi}^2 \leq \|\mathbf{a}\|_p \tilde{L}_{\Phi}^2 = \delta \tilde{L}_{\Phi}^2. \quad (58)$$

1132 Plugging the result back into (13) yields the desired result. □

1133 **Lemma A.5.** *Under the conditions described in Theorem 3.2, $R_p(\epsilon) \rightarrow 0$ as $\epsilon \rightarrow 0$ for $p \in \{2, \infty\}$.*

1134 *Proof.* $p = \infty$: Due to the definition of compressibility, for all $l \in [\lambda]$,

$$1136 \quad \|\boldsymbol{\nu}^l - \boldsymbol{\nu}_k^l\|_1 \leq \epsilon \|\boldsymbol{\nu}^l\|_1 \quad (59)$$

$$1137 \quad \nu_{k+1}^l \leq \epsilon h \|\mathbf{W}^l\|_F, \quad (60)$$

1139 by applying standard norm inequalities across rows and columns. The result follows from noting that
1140 the final inequality applies to both ν_{k+1}^l and ν_{k+1}^{l+1} .
1141

1142 $p = 2$: Similarly, due to the definition of compressibility, for all $l \in [\lambda]$,

$$1143 \quad \|\boldsymbol{\sigma}^l - \boldsymbol{\sigma}_k^l\|_1 \leq \epsilon \|\boldsymbol{\sigma}^l\|_1 \quad (61)$$

$$1144 \quad \sigma_{k+1}^l \leq \epsilon \sqrt{h} \|\mathbf{W}^l\|_F, \quad (62)$$

1146 since $\|\boldsymbol{\sigma}^l\|_2 = \|\mathbf{W}^l\|_F$. The result follows from noting that the final inequality applies to both σ_{k+1}^l
1147 and σ_{k+1}^{l+1} . \square
1148

1149 **Lemma A.6.** *Under the conditions described in Theorem 3.2, $A_p^*(\mathbf{W}^{l+1}, \mathbf{W}^l) \leq 1$ for $p \in \{2, \infty\}$.*

1152 *Proof.* For $p = \infty$,

$$1153 \quad A_\infty^*(\mathbf{W}^{l+1}, \mathbf{W}^l) = \max_{\mathbf{D} \in \mathcal{D}} \frac{\|\mathbf{W}^{l+1} \mathbf{D} \mathbf{W}^l\|_\infty}{\|\mathbf{W}^{l+1}\|_\infty \|\mathbf{W}^l\|_\infty} \quad (63)$$

$$1154 \quad \leq \frac{\|\mathbf{W}^{l+1}\|_\infty \max_{\mathbf{D} \in \mathcal{D}} \|\mathbf{D}\|_\infty \|\mathbf{W}^l\|_\infty}{\|\mathbf{W}^{l+1}\|_\infty \|\mathbf{W}^l\|_\infty} \quad (64)$$

$$1155 \quad \leq \frac{\|\mathbf{W}^{l+1}\|_\infty \|\mathbf{W}^l\|_\infty}{\|\mathbf{W}^{l+1}\|_\infty \|\mathbf{W}^l\|_\infty} = 1. \quad (65)$$

1160 The proof follows identically for $p = 2$. \square

B ADDITIONAL TECHNICAL RESULTS AND ANALYSES

B.1 (q, k, ϵ) -COMPRESSIBILITY VS. OTHER NOTIONS OF APPROXIMATE SPARSITY

Further discussion of (q, k, ϵ) -compressibility.

1169 Our concept of compressibility can be thought of as the generalization of *sparsity*, with the obvious
1170 advantage of being applicable to domains where true sparsity is rare, such as neural network parameter
1171 values. Note that our intuitive definition of compressibility is based on foundational results in
1172 compressed sensing and is well exploited in the established machine learning literature (Amini
1173 et al., 2011; Gribonval et al., 2012; Barsbey et al., 2021; Diao et al., 2023; Wan et al., 2024). More
1174 specifically, when $k \ll d$ and $\epsilon \ll 1$, Definition 2.1 is equivalent to Gribonval et al. (2012)'s definition
1175 of *compressible vector*. Inspired by desiderata from an ideal metric of sparsity in the economics
1176 literature, Diao et al. (2023) recently introduced another scale-invariant notion of approximate
1177 sparsity:

1178 **Definition B.1** (PQ Index Diao et al. (2023)). *For any $0 < p < q$, the PQ Index of a non-zero vector
1179 $\mathbf{w} \in \mathbb{R}^d$ is*

$$1180 \quad I_{p,q}(\mathbf{w}) = 1 - d^{\frac{1}{q} - \frac{1}{p}} \frac{\|\mathbf{w}\|_p}{\|\mathbf{w}\|_q}. \quad (66)$$

1182 Interestingly, it is possible to directly relate this notion of sparsity to (q, k, ϵ) -compressibility, as
1183 shown in the following proposition.

1184 **Proposition B.2.** *Given $0 < p < q$, for a vector $\boldsymbol{\theta}$, its (q, k, ϵ) compressibility implies the following
1185 lower bound for its PQ Index:*

$$1186 \quad 1 - \epsilon - \kappa^\phi \leq I_{p,q}(\boldsymbol{\theta}), \quad (67)$$

1187 where $\kappa = k/d$ and $\phi = \frac{1}{p} - \frac{1}{q}$. Note that the constraints on p, q imply $\phi > 0$.

1188 *Proof.* Let $\gamma = \frac{1}{p} - \frac{1}{q}$. Note that from (12) we know that $\|\boldsymbol{\theta}\|_p \leq (k^\gamma + d^\gamma \epsilon) \|\boldsymbol{\theta}\|_q$. This implies
 1189

$$\frac{\|\boldsymbol{\theta}\|_p}{\|\boldsymbol{\theta}\|_q} \leq k^\gamma + d^\gamma \epsilon. \quad (68)$$

1190 Note that PQ Index from (66) can be written as $(1 - I_{p,q}(\boldsymbol{\theta}))d^\gamma = \frac{\|\boldsymbol{\theta}\|_p}{\|\boldsymbol{\theta}\|_q}$. Plugging this into the LHS
 1191 of (68) and simple algebraic manipulation gives the desired result. \square
 1192

1193 *Remark B.3.* Assume that $\boldsymbol{\theta}$ and $\boldsymbol{\theta}'$ are (q, k, ϵ) and (q, k', ϵ') compressible respectively. If $k = k'$
 1194 and $\epsilon < \epsilon'$; or $k < k'$ and $\epsilon = \epsilon'$ implies a larger lower bound on PQI. That is, a larger (q, k, ϵ)
 1195 compressibility suggests a larger PQI.
 1196

1197 **Dominance vs. spread.** While (q, k, ϵ) -compressibility quantifies how well a vector can be approximated using its top- k entries (e.g. top- k filters or singular values), it does not fully capture the internal structure among those dominant terms. Consider the vectors $\mathbf{x}_1 = (10, 2, 1, 1)$ and $\mathbf{x}_2 = (6, 6, 1, 1)$: both yield the same 2-term relative approximation error under $q = 1$, yet their dominant components differ markedly in structure. To formalize this distinction, we introduce the **spread variable** as
 1198 a complementary descriptor. Given a vector $\boldsymbol{\theta}$ with elements sorted by magnitude, we define its
 1199 *spread* $\beta \in [0, 1]$ via the relation $|\theta_k| = (1 - \beta)|\theta_1|$. Intuitively, β quantifies the relative decay
 1200 from the largest to the k -th largest entry, capturing an additional degree of freedom in the geometry
 1201 of compressibility, better describing and distinguishing compressible distributions beyond what is
 1202 possible with approximation error alone.
 1203

1204 Lastly, to provide a numerical comparison, consider $\mathbf{x}_1 = (6.00, 1.50, 0.75, 0.75)$ and $\mathbf{x}_2 =$
 1205 $(4.00, 4.00, 0.057, 0.057)$. The qualitative difference between the two vectors is obvious, and is easy
 1206 to observe under our compressibility definition: with $q = 2, k = 2$, we have $\epsilon = 0.169, \beta = 0.75$
 1207 vs. $\epsilon = 0.014, \beta = 0.00$, respectively. Note that this difference is captured neither by the classical
 1208 notion of sparsity (neither vector includes any 0 elements), nor the more modern PQ Index, as both
 1209 vectors have a PQI(2, 1) of 0.697.
 1210

1214 B.2 LOWER BOUNDS ON OPERATOR NORMS

1215 The following theorem characterizes the compressibility-based lower bounds of operator norms,
 1216 complementing the upper bounds presented in the main paper.
 1217

1218 **Theorem B.4.** *The following statements lower bound operator norms using compressibility and
 1219 Frobenius norm.*

1220 (a) **Neuron compressibility (i.e. row-sparsity):** Let $\mathbf{w}_i, i \in [h]$ denote the rows of the matrix \mathbf{W} ,
 1221 and let $\boldsymbol{\nu} := (\|\mathbf{w}_1\|_1, \dots, \|\mathbf{w}_h\|_1)$ denote ℓ_1 norms of its rows. Assuming $\boldsymbol{\nu}$ is $(1, k_{\boldsymbol{\nu}}, \epsilon_{\boldsymbol{\nu}})$ and
 1222 each row \mathbf{w}_i is $(2, k_r, \epsilon_r)$ compressible implies:

$$\left(\frac{\sqrt{k_r}}{\sqrt{k_r(1 - \epsilon_r^2)} + \sqrt{\epsilon_r}} \right) \frac{(1 - \epsilon_{\boldsymbol{\nu}})}{k_{\boldsymbol{\nu}}} \|\mathbf{W}\|_F \leq \|\mathbf{W}\|_{\infty}. \quad (69)$$

1223 (b) **Spectral compressibility (i.e. low-rankness):** Let $\boldsymbol{\sigma} := (\sigma_1, \sigma_2, \dots)$ denote the singular values
 1224 of matrix \mathbf{W} . Assuming $\boldsymbol{\sigma}$ is $(1, k_{\boldsymbol{\sigma}}, \epsilon_{\boldsymbol{\sigma}})$ compressible implies:

$$\sqrt{\frac{(1 - h\epsilon_{\boldsymbol{\sigma}}^2)}{k_{\boldsymbol{\sigma}}}} \|\mathbf{W}\|_F \leq \|\mathbf{W}\|_2. \quad (70)$$

1225 *Proof.* For (a) note that $\|\mathbf{W}\|_{\infty} = \|\boldsymbol{\nu}\|_{\infty}$. Note that the minimum value this value can take is
 1226 $\|\boldsymbol{\nu}_k\|_1/k_{\boldsymbol{\nu}}$. By the definition of strict compressibility, we know that $\|\boldsymbol{\nu}_k\|_1 = (1 - \epsilon)\|\boldsymbol{\nu}\|_1$. This gives
 1227 us the inequality:

$$\frac{(1 - \epsilon_{\boldsymbol{\nu}})}{k_{\boldsymbol{\nu}}} \|\boldsymbol{\nu}\|_1 \leq \|\mathbf{W}\|_{\infty}. \quad (71)$$

1228 We then turn to the components of $\boldsymbol{\nu}$, and examine the relationship between $\|\mathbf{w}\|_2$ and $\|\mathbf{w}\|_1$ for any
 1229 row \mathbf{w} . We will use $\mathbf{w}_k, \mathbf{w}_r$ to refer to the dominant and remainder terms of \mathbf{w} respectively. We
 1230 invoke Minkowski's inequality:
 1231

$$\|\mathbf{w}\|_2 \leq \|\mathbf{w}_k\|_2 + \|\mathbf{w}_r\|_2. \quad (72)$$

We bound the leftmost term by $\|\mathbf{w}_k\|_2 \leq \sqrt{1 - \epsilon_r^2} \|\mathbf{w}\|_2 \leq \sqrt{1 - \epsilon_r^2} \|\mathbf{w}\|_1$ due to Lemma A.1. For the term $\|\mathbf{w}_r\|_2$, we observe that due to interpolation inequality:

$$\|\mathbf{w}_r\|_2 \leq \|\mathbf{w}_r\|_1^{\frac{1}{2}} \|\mathbf{w}_r\|_{\infty}^{\frac{1}{2}}. \quad (73)$$

Examining $\|\mathbf{w}_r\|_{\infty}$, we note that the maximum magnitude \mathbf{w}_r can contain is less than or equal to the maximum value the lowest magnitude element of \mathbf{w}_k can take. This is the case when all elements of \mathbf{w}_k are equal, therefore $\|\mathbf{w}_r\|_{\infty} \leq \|\mathbf{w}_k\|_1/k$. Using this, the fact that $\|\mathbf{w}_k\|_1 \leq \|\mathbf{w}\|_1$, and that $\|\mathbf{w}_r\|_1 \leq \epsilon \|\mathbf{w}\|_1$ by compressibility definition, we can write:

$$\|\mathbf{w}_r\|_2 \leq \|\mathbf{w}_r\|_1^{\frac{1}{2}} \|\mathbf{w}_r\|_{\infty}^{\frac{1}{2}} \leq \epsilon^{\frac{1}{2}} \|\mathbf{w}\|_1^{\frac{1}{2}} \left(\frac{\|\mathbf{w}\|_1}{k} \right)^{\frac{1}{2}} \leq \frac{\sqrt{\epsilon}}{\sqrt{k}} \|\mathbf{w}\|_1,$$

Plugging this back into the additive decomposition of $\|\mathbf{w}\|_2$ above, we have:

$$\frac{\sqrt{k}}{\sqrt{k(1 - \epsilon^2)} + \sqrt{\epsilon}} \|\mathbf{w}\|_2 \leq \|\mathbf{w}\|_1. \quad (74)$$

Let $\hat{\boldsymbol{\nu}}$ denote the ℓ_2 norms of \mathbf{W} 's rows. Then, plugging this back to the main inequality:

$$\|\mathbf{W}\|_{\infty} \geq \frac{(1 - \epsilon_{\boldsymbol{\nu}})}{k_{\boldsymbol{\nu}}} \|\boldsymbol{\nu}\|_1. \quad (75)$$

$$\geq \frac{\sqrt{k}}{\sqrt{k(1 - \epsilon^2)} + \sqrt{\epsilon}} \frac{(1 - \epsilon_{\boldsymbol{\nu}})}{k_{\boldsymbol{\nu}}} \|\hat{\boldsymbol{\nu}}\|_1 \quad (76)$$

$$\geq \frac{\sqrt{k}}{\sqrt{k(1 - \epsilon^2)} + \sqrt{\epsilon}} \frac{(1 - \epsilon_{\boldsymbol{\nu}})}{k_{\boldsymbol{\nu}}} \|\hat{\boldsymbol{\nu}}\|_2 \quad (77)$$

$$\geq \frac{\sqrt{k}}{\sqrt{k(1 - \epsilon^2)} + \sqrt{\epsilon}} \frac{(1 - \epsilon_{\boldsymbol{\nu}})}{k_{\boldsymbol{\nu}}} \|\mathbf{W}\|_F \quad (78)$$

which gives use the desired inequality.

For (b), we will use $\boldsymbol{\sigma}_k$, $\boldsymbol{\sigma}_r$ to refer to the dominant and remainder terms of $\boldsymbol{\sigma}$ respectively. Note that $\|\mathbf{W}\|_F^2 = \|\boldsymbol{\sigma}\|_2^2 = \|\boldsymbol{\sigma}_k\|_2^2 + \|\boldsymbol{\sigma}_r\|_2^2$. We bound the norm of the dominant singular values by $\|\boldsymbol{\sigma}_k\|_2^2 \leq k \boldsymbol{\sigma}_1^2 = k \|\mathbf{W}\|_2^2$. We bound the remainder singular values by noting that

$$\|\boldsymbol{\sigma}_r\|_2^2 \leq (\|\boldsymbol{\sigma}_r\|_1)^2 \leq (\epsilon_{\boldsymbol{\sigma}} \|\boldsymbol{\sigma}\|_1)^2 \leq \epsilon_{\boldsymbol{\sigma}}^2 (\sqrt{h} \|\boldsymbol{\sigma}\|_2)^2 = h \epsilon_{\boldsymbol{\sigma}}^2 \|\mathbf{W}\|_F^2. \quad (79)$$

This gives us the inequality:

$$\|\mathbf{W}\|_F^2 \leq k \|\mathbf{W}\|_2^2 + h \epsilon_{\boldsymbol{\sigma}}^2 \|\mathbf{W}\|_F^2. \quad (80)$$

Rearranging the terms gives the desired lower bound. \square

B.3 RELATIONSHIPS BETWEEN OPERATOR NORMS

Although Theorem 3.1 directly relates ℓ_{∞} and ℓ_2 operator norms to neuron and spectral compressibility, both the known norm inequality relationships and our results on cross-norm adversarial attacks imply that these two quantities are likely to be strongly correlated under this context. We conduct simple experiment to test this hypothesis: We optimize for either ℓ_{∞} or ℓ_2 operator norm of a random i.i.d. Gaussian matrix \mathbf{A} where $A_{i,j} \stackrel{\text{i.i.d.}}{\sim} \mathcal{N}(0, 1)$. We then conduct a gradient ascent-based optimization of the matrix's either ℓ_{∞} or ℓ_2 operator norms, while normalizing the Frobenius norm to its initialization value. In Figure 9, as an average of 10 random seeds, we show how ℓ_{∞} and ℓ_2 evolve while either ℓ_{∞} (top) and ℓ_2 (bottom) are optimized. We note that in both case both norms are strongly associated in increasing simultaneously. Note that given the inequality $\|\mathbf{A}\|_2 \leq \|\mathbf{A}\|_F$, by the end of optimization the spectral norm reaches its limit in Frobenius norm. While the left column shows the norms across iterations, center and right columns portray the qualitative differences produced by optimizing for either columns. As expected, optimizing for ℓ_{∞} collects all energy in a single row, while optimizing for ℓ_2 produces a 1-rank matrix.

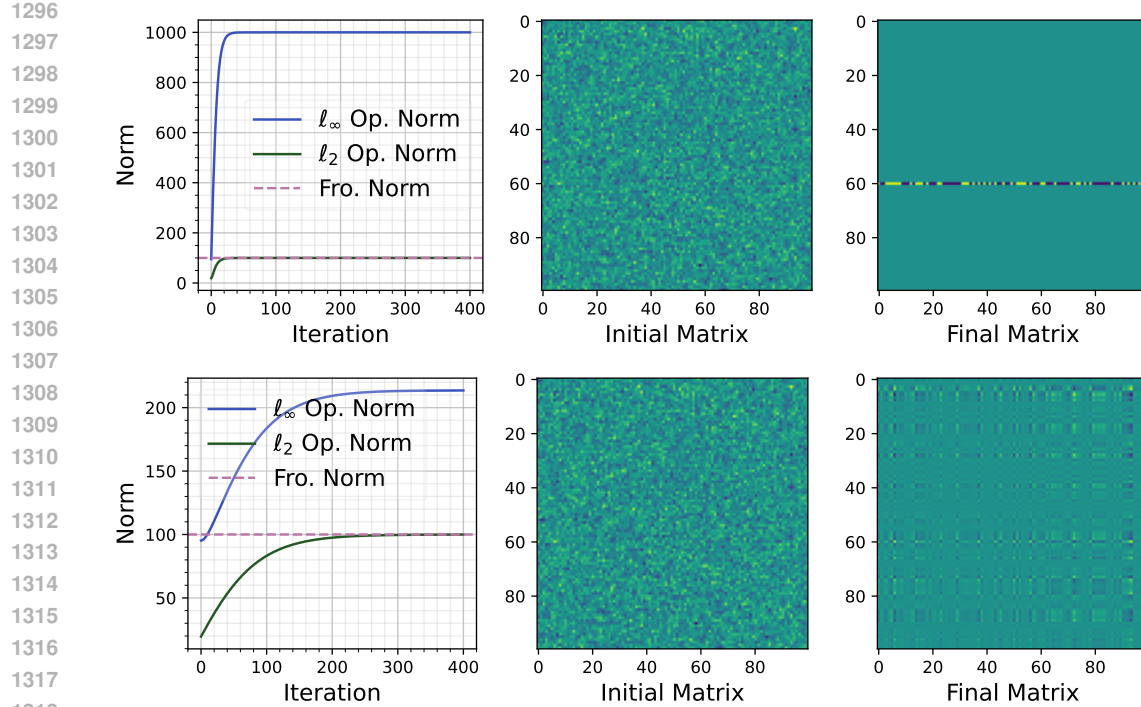
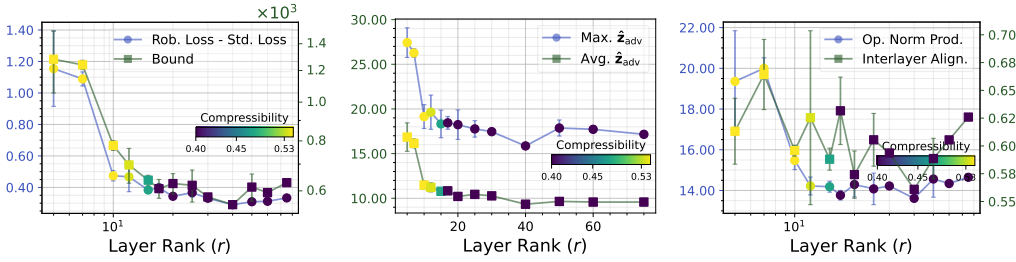
Figure 9: Optimizing for ℓ_∞ (top) and ℓ_2 (bottom) operator norms.

Figure 10: Empirically investigating the implications of Theorem 3.2.

B.4 EMPIRICAL ANALYSES OF THE ROBUSTNESS BOUND AND RELATED QUANTITIES

In this section, we directly investigate how well our bound correlates with the adversarial robustness gap, as predicted in Corollary 3.3. In order to fully conform to the setting of Corollary 3.3, we convert the previously introduced MNIST dataset to a binary classification task by converting its labels to 0-1, by assigning 0-4 to class 0 and 5-9 to class 1. We create a fully connected network (FCN) with two hidden layers of width 300, with ReLU activations after each layer. We then create networks with various spectral compressibility through varying the rank of the hidden layers, imposed through low-rank factorization. While computing the bound, we determine k (num. dominant terms), and compute ϵ and β as statistics. Note that if $\beta = 1$, this would make the bound undefined - however, instead of being a numerical problem, this implies that k should be selected lower, as dominant terms including 0 is an undesired corner case. Figure 10 demonstrates the results of our experiment. First, Figure 10 (left) shows that our bound is closely correlated with adversarial robustness gap. This shows that although our bound is an order of magnitude above the empirical loss difference, it is still a faithful indicator of adversarial robustness.

We then investigate whether local input sensitivity of the network tracks its global properties. As in the main paper, letting $z = \Phi(x)$ and $z_{\text{adv}} = \Phi(x + \mathbf{a}^*)$ denote the learned representations of clean and perturbed input images, we compute $\|z - z_{\text{adv}}\|_2 / \|\mathbf{a}^*\|_2$ for 1000 test samples. We

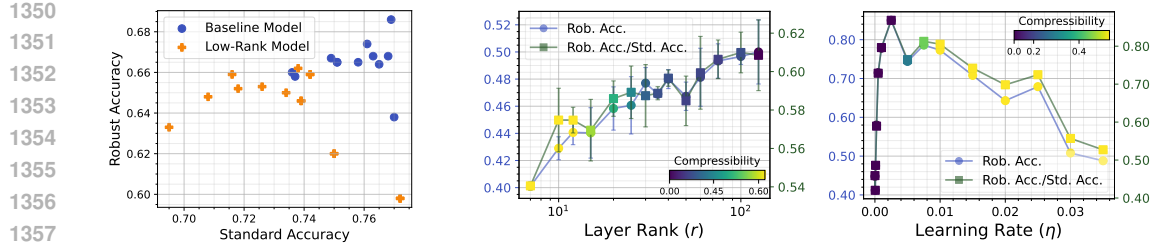


Figure 11: Adversarial fine-tuning (left) and training (center). Robust accuracy under increasing learning rate (right).

take this metric as a secant approximation of the local Lipschitz constant around input x . We then use the maximum and the mean of this statistic over the samples as *empirical lower bounds* to the global and expected local Lipschitz constants respectively. Figure 10 (center) shows that these two values are closely correlated: An increase in the maximum sensitivity to perturbation is reflected in a similar increase in the average sensitivity. Lastly, Figure 10 (right) investigates the effect of spectral compressibility on interlayer alignment, in parallel to product of spectral norms of the layers (to quantify the intra- vs. interlayer dynamics in our bound). Results show that while norms increase as expected, interlayer alignment does not necessarily portray a consistent pattern. We consider how and why interlayer alignment changes in response to various compressibility inducing sparsity and training dynamics to be a crucial future research direction.

B.5 APPROXIMATING THE INTERLAYER ALIGNMENT TERMS

Note that the interlayer alignment terms used in Theorem 3.2 lead to a combinatorial optimization problem due to the discreteness of ReLU gradients, i.e. $\{0, 1\}$. A closely related precedent from the literature is SeqLip by Scaman & Virmaux (2018), with the differences relating to the normalization of the terms, and the k -term adaptation. However, since these differences do not lead to any changes with respect to the optimization of these terms (*i.e.* their maxima), the authors' approximation methodology is an attractive choice for determining A_p^* . Scaman & Virmaux (2018) report that their gradient-ascent based greedy search algorithm is in $\sim 1\%$ of the analytical solution for cases where the latter is computationally feasible. We adopt their solution to our case for both interlayer alignment terms.

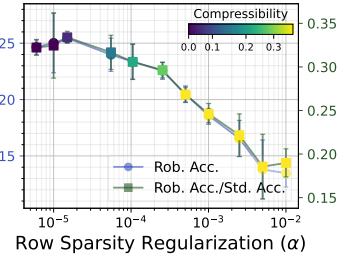


Figure 12: Effects of standard group lasso on compressibility and adversarial robustness.

1404 C DETAILS OF THE EXPERIMENTAL SETTINGS

1405 C.1 DATASETS

1408 Our experiments are conducted using the most commonly utilized datasets and ar-
 1409 chitectures in research on adversarial robustness under pruning (Piras et al., 2025).
 1410 Our datasets include MNIST (Deng, 2012), CIFAR-10, CIFAR-100
 1411 (Krizhevsky & Hinton, 2009), SVHN (Netzer et al., 2011), Flickr30k (Young
 1412 et al., 2014), and ImageNet-1k (Deng
 1413 et al., 2009). As detailed in Appendix B,
 1414 we convert MNIST into a binary
 1415 classification task for empirically
 1416 investigating how our bound correlates
 1417 with adversarial robustness gap. In all
 1418 datasets, we use the canonical train-test
 1419 splits. Whenever validation set-based
 1420 model selection or early stopping is
 1421 used, we utilize 5% of the training set
 1422 for this task, and conduct early stopping
 1423 with a patience of 10 epochs based on
 1424 validation loss.

1425 C.2 MODELS

1428 Architectures we utilize include fully connected networks
 1429 (FCN), ResNet18 (He et al., 2016), VGG16 (Simonyan & Zis-
 1430 sserman, 2014), WideResNet-101-2 (Zagoruyko & Komodakis,
 1431 2016), vision transformer (ViT) - both as a standalone classi-
 1432 fier (Dosovitskiy et al., 2021) and as part of a CLIP encoder
 1433 (Radford et al., 2021), and Swin Transformer (Liu et al., 2021).
 1434 Whenever needed, we apply modifications to the standard ar-
 1435 chitectures in question. For our visualization experiments at
 1436 the beginning of Section 4, we utilize a 1-hidden layer FCN
 1437 with ReLU activation, with no bias nodes, and a width of 400.
 1438 For our main results with CIFAR-10, we utilize a 2000-width
 1439 FCN with 4 hidden layers, with the remaining architectural
 1440 choices remain identical. Regarding the VGG16 architecture,
 1441 due to our datasets being size 32×32 , we remove the redundant
 1442 4096-width linear layers (along with their interleaving
 1443 dropout and ReLU layers). Lastly, when conducting the low-
 1444 rank factorization experiments, we modify linear layers with
 1445 a factorized layer, and do the equivalent for 2D convolutional
 1446 layers (Zhong et al., 2023).

1447 For transformer models, we utilize a Base ViT architecture with 8×8 patch size. When fine-tuning a
 1448 pre-trained version, we utilize a version pretrained on ImageNet-21K and fine-tuned on ImageNet-1K,
 1449 hosted by the HuggingFace platform (Wolf et al., 2020). For the Swin Transformer we use a tiny
 1450 version of the architecture, and utilize an ImageNet-1K pretrained version hosted by torchvision
 1451 (maintainers & contributors, 2016). For CLIP experiments, we utilize a pre-trained CLIP model, CLIP
 1452 ViT-B/32, trained on LAION 2B dataset, hosted by Open CLIP (Ilharco et al., 2021). To conduct
 1453 the zero-shot classification with the fine-tuned CLIP, we fine-tune the dataset with the Flickr30k
 1454 dataset using a weight decay of 0.01 and a learning rate of $1e-5$ for 30 epochs. For the classification
 1455 that follows, we present results with top-5 (standard and adversarial) accuracy, and we utilize the
 following prompts to embed the text descriptions, which serve as the class vectors:

- a photo of a ...
- a blurry photo of a ...

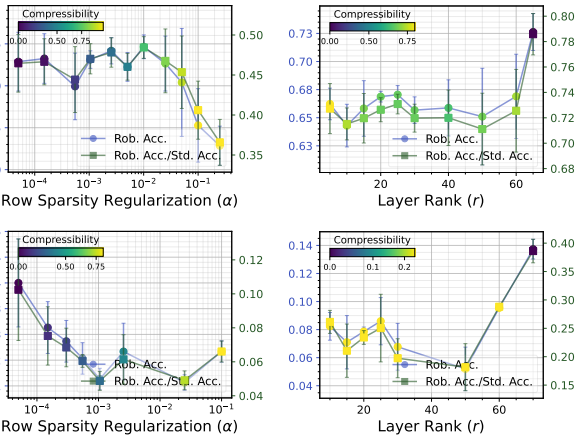


Figure 13: Results with SVHN & Wide ResNet 101-2 (top),
 CIFAR-100 & VGG16 (bottom).

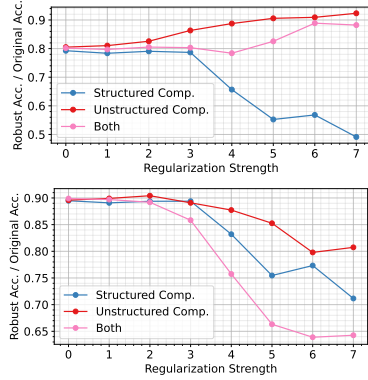


Figure 14: Unstructured alongside structured comp., for row sparsity (top) and spectral comp. (bottom).

1458 • a photo of the ...
 1459 • a close-up photo of a ...
 1460 • a black and white photo of a ...
 1461 • a cropped photo of a ...
 1462 • a bright photo of a ...
 1463

1464

1465 C.3 STANDARD AND ADVERSARIAL TRAINING

1466

1467 **Standard training.** We normally use softmax cross-entropy loss, the AdamW optimizer with a
 1468 weight decay of 0.01, a learning rate of 0.001, and use validation set based model selection for early
 1469 stopping. For adversarial training tasks, we also include a cosine learning rate annealing schedule
 1470 (epochs = 60, min. learning rate = 0), basic data augmentation in the form of random cropping and
 1471 horizontal flips, and an adversarial validation set, again constituting 10% of the training set.

1472 **Evaluating and training for adversarial robustness.** For evaluating adversarial robustness, we
 1473 primarily employ the AutoPGD attack (Croce & Hein, 2020), using the implementation from Nicolae
 1474 et al. (2018). During adversarial training, we generate adversarial examples at each iteration using the
 1475 PGD attack (Madry et al., 2018). Unless stated otherwise, adversarial examples make up 50% of each
 1476 training minibatch. For models trained end-to-end with adversarial robustness, we set $\epsilon = 8/255$ for
 1477 ℓ_∞ attacks and $\epsilon = 0.5$ for ℓ_2 attacks. For standard or adversarially fine-tuned models, we use 25%
 1478 of these budgets to enable a clear comparison.

1479

1480 C.4 IMPLEMENTATION AND HARDWARE

1481

1482 **Implementation.** We utilize the Python programming language and PyTorch deep learning framework
 1483 for our implementation (Paszke et al., 2019). Whenever possible, we utilize the default torchvision
 1484 (maintainers & contributors, 2016) implementations of our models - we modify these baselines for the
 1485 changes mentioned above. For adversarial training and evaluation, we use the Adversarial Robustness
 1486 Toolbox (Nicolae et al., 2018). Our source code provides further details regarding implementation, to
 1487 be made publicly available upon publication.

1488 **Hardware and resources.** All experiments are conducted on the computational server of an institute,
 1489 utilizing Nvidia L40S GPUs. The main paper experiments took a total of 600 GPU hours to complete,
 1490 including ≥ 3 seed replication for the main results. Total development time is estimated to be $3.5 \times$
 1491 of the compute time for the final publication.

1492

1493 D ADDITIONAL EMPIRICAL RESULTS

1494

1495 D.1 EXPERIMENTS WITH OTHER DATASETS AND ARCHITECTURES

1496 As mentioned in the main paper, we now extend our empirical findings to other datasets and archi-
 1497 tec tures. Figure 13 demonstrates results with SVHN dataset and Wide ResNet 101-2 architecture
 1498 (top), and CIFAR-100 dataset and VGG16 architecture (bottom). Our results replicate with novel
 1499 datasets and architectures, as qualitatively identical results are obtained in these alternative settings.

1500 Note that the slight initial increase under neuron compressibility seen with WideResNet 101-2 here
 1501 and ResNet18 in the main paper cannot be seen with VGG16, highlighting the regime dependence of
 1502 multiple inductive biases compressibility-inducing regularizations might have.

1503

1504 D.2 GROUP SPARSITY REGULARIZATION

1505

1506 In the main paper, we highlight that we utilize a scale-invariant version of group lasso to disentangle
 1507 the downstream effects of increasing compressibility vs. decreasing overall parameter scale. Figure 12
 1508 replicates our main results on ResNet18 and CIFAR-10 while using standard group lasso regular-
 1509 ization. While its effects are mostly similar to our version of group lasso, we note that Figure 12
 1510 presents a subtle difference, where group lasso first creates a slight but statistically significant (error
 1511 bars = 1 std. deviation) increase in robustness at very low levels. However, as indicated in the main
 1512 text, these benefits are overtaken by the negative effects of row compressibility as regularization
 1513 strength increases.

1512
1513

D.3 ADVERSARIAL TRAINING RESULTS FOR SPECTRAL COMPRESSIBILITY

1514
1515
1516
1517
1518
1519
1520

Figure 11 (left, center) presents the spectral compressibility counterpart for adversarial fine-tuning and training results from the main paper, under ℓ_2 adversarial attacks. The patterns clearly mirror those presented in the main paper under row sparsity conditions.

1521
1522D.4 COMPRESSIBILITY
THROUGH INDUCTIVE BIAS1523
1524

We now examine whether the results we have observed with explicit regularization methods also apply to cases when compressibility is obtained through the inductive bias of the learning algorithm. For this, we go back to the setting presented in Appendix B, and instead of increasing regularization hyperparameter, we increase initial learning rate (η) of the training algorithm. The results, presented Figure 11 (right), paint an intriguing picture. While initially increasing η improves adversarial robustness under ℓ_∞ attacks (perhaps paralleling its well-known benefits for standard generalization), as soon as it starts to increase row compressibility, its benefits of η quickly disappear. This highlights the fact that our results not only inform the adversarial robustness behavior under explicit regularization and architecture design, but also inductive biases of the learning algorithm.

1537

1538
1539

D.5 UNSTRUCTURED COMPRESSIBILITY

1540

While unstructured compressibility is not the focus of our study, we note that it appears in the bound for L_Φ^∞ in Theorem 3.2, unlike that for L_Φ^2 . To investigate the significance of this result, we replicate the setting presented in Appendix B, but this time in addition to increasing the group lasso/nuclear norm regularization, we run a separate set of experiments where we either solely increase L1 regularization, or increase it along with structured sparsity-inducing regularization. We then compare the performance of the resulting models under the corresponding adversarial attacks. The results are presented in Figure 14. Remember that our bound implies *positive* effects of unstructured compressibility for L_Φ^∞ . Indeed, in Figure 14 we see that L1 regularization can compensate for the negative effects of structured compressibility (top), while it has no such benefits for spectral compressibility (bottom). We believe that understanding the intricate relationships among different types of compressibility is a crucial future research direction.

1561

1562
1563

D.6 RESULTS WITH ALTERNATIVE NORMS, BUDGETS, AND ATTACKS

1564
1565

While for brevity we presented our main results to include robustness against ℓ_∞ attacks under neuron sparsity, and ℓ_2 attacks under spectral compressibility, for completeness we provide our central results with the cross-norm attacks, *i.e.* ℓ_∞ attacks under spectral compressibility, and ℓ_2 attacks under neuron

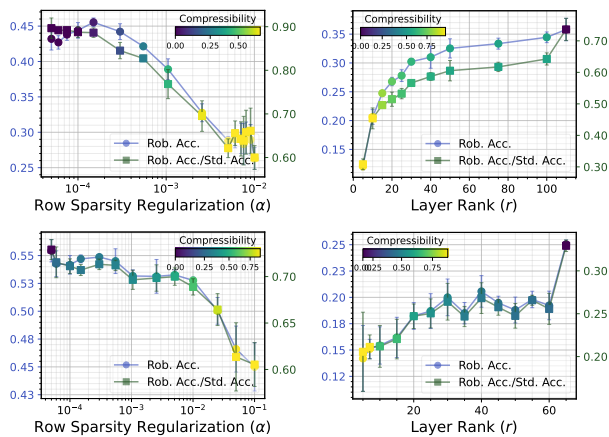


Figure 15: Results with CIFAR-10, FCN (top) and ResNet18 (bottom), with alternative attack norms to Figure 5.

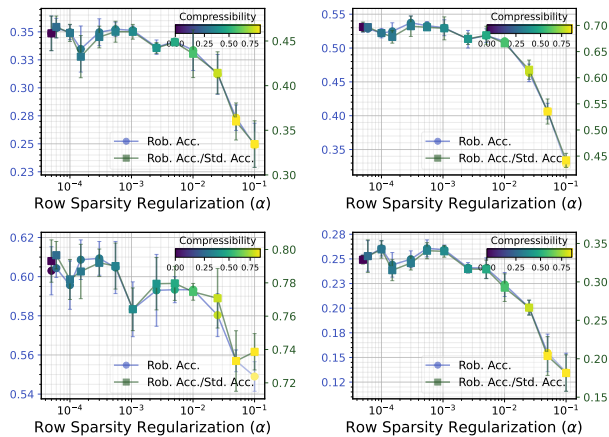


Figure 16: Results on CIFAR-10, ResNet18 and attacks with FGSM (top left), AutoCG (top right), Square Attack (bottom left), and AutoAttack (bottom right).

1566 sparsity. The results are presented in Figure 15, and are fully in line with the results presented in the
 1567 main paper.

1568 **Model performance under varying attack budgets.** As described in the main paper, in order to
 1569 investigate the effects of structural interventions on standard trained models’ adversarial robustness,
 1570 we utilize a smaller attack budget to avoid floor effects from obscuring the effects we are investigating.
 1571 Table 1 demonstrates that our results are not dependent on a specific attack budget, and the patterns
 1572 that confirm our hypotheses hold across various attack budgets; however in standard trained models
 1573 floor effects indeed prevent the observation of the results of our interventions, justifying our utilization
 1574 of a reduced budget in such cases.

1575
 1576 Table 1: Robust accuracy of a ViT model trained on CIFAR-10, under increasing adversarial sample
 1577 ratio in training (ρ) vs. increasing ℓ_∞ attack budgets (ϵ).

	$\rho = 0.0$	$\rho = 0.05$	$\rho = 0.1$	$\rho = 0.25$	$\rho = 0.5$
$\epsilon = 2/255$	0.111	0.333	0.479	0.519	0.510
$\epsilon = 4/255$	0.002	0.061	0.263	0.371	0.390
$\epsilon = 8/255$	0.000	0.002	0.032	0.113	0.179
$\epsilon = 16/255$	0.000	0.000	0.000	0.005	0.019

1584
 1585 **Model performance under alternative attacks.** We investigate whether our results replicate under
 1586 alternative attacks. We therefore repeat our experiments with ResNet18 and CIFAR-10 in the main
 1587 paper with FGSM (Goodfellow et al., 2015), AutoCG (Yamamura et al., 2022), Square Attack
 1588 (Andriushchenko et al., 2020), and the composite AutoAttack (Croce & Hein, 2020); as opposed to
 1589 the original AutoPGD. Results in Figure 16 confirm that our results are qualitatively identical under
 1590 different attacks.

1591 D.7 FINE-TUNING RESULTS WITH TRANSFORMERS

1593 As described in the main text and above, we investigate whether we can replicate our results while
 1594 fine-tuning ImageNet-pretrained transformer models, ViT and Swin Transformer, on CIFAR-10 and
 1595 SVHN respectively, while utilizing sparsification regularization. The results are presented in Table 2
 1596 and Table 3, and replicate our hypotheses.

1597
 1598 Table 2: Robust and standard accuracies of pretrained ViT models fine-tuned on CIFAR-10 dataset
 1599 under varying neuron sparsification regularization strength (α), i.e. group lasso.

	$\alpha = 0.0$	$\alpha = 0.001$	$\alpha = 0.005$	$\alpha = 0.01$	$\alpha = 0.05$	$\alpha = 0.1$
Rob. Acc.	0.383	0.362	0.369	0.219	0.123	0.111
Std. Acc.	0.920	0.926	0.921	0.893	0.873	0.829
RA/SA	0.416	0.401	0.391	0.245	0.141	0.134

1605
 1606 Table 3: Robust and standard accuracies of pretrained Swin Transformer models fine-tuned on SVHN
 1607 dataset under varying neuron sparsification regularization strength (α).

	$\alpha = 0.0$	$\alpha = 0.001$	$\alpha = 0.005$	$\alpha = 0.01$	$\alpha = 0.05$	$\alpha = 0.1$
Rob. Acc.	0.384	0.360	0.357	0.326	0.155	0.083
Std. Acc.	0.889	0.877	0.887	0.880	0.881	0.875
RA/SA	0.432	0.410	0.402	0.370	0.176	0.095

1613 Given that classification accuracy is the most commonly utilized and communicated metric in the
 1614 literature on adversarial robustness, the main paper reports these as our primary metric. However, we
 1615 find that same hypothesized patterns can be observed when robust loss - standard loss is utilized as the
 1616 main metric, instead of accuracy. Table 4 demonstrates these results in the fine-tuning experiments
 1617 described above, replicating our findings with robust and standard accuracy.

1618 D.8 RESULTS WITH POST-PRUNING FINE-TUNING

1620
1621 Table 4: Robust and standard accuracies and loss differences for pretrained Swin Transformer models
1622 fine-tuned on SVHN dataset under varying neuron sparsification regularization strength (α).
1623

	$\alpha = 0.0$	$\alpha = 0.001$	$\alpha = 0.005$	$\alpha = 0.01$	$\alpha = 0.05$	$\alpha = 0.1$
Rob. Acc.	0.384	0.360	0.357	0.326	0.155	0.083
Std. Acc.	0.889	0.877	0.887	0.880	0.881	0.875
Adv. Loss - Test Loss	0.505	0.517	0.530	0.554	0.726	0.792

1627
1628 Utilizing a baseline model adversarially trained on CIFAR-10 dataset with
1629 ResNet18 architecture, instead of regularizing for compressibility, we prune and
1630 then fine tune our models to investigate
1631 1- whether the main paper’s results will
1632 replicate under post-pruning fine-tuning,
1633 2- whether fine-tuning procedure will be
1634 another source of vulnerability in and of
1635 itself.
1636

1637 After layerwise structured pruning, we fine-tune the models
1638 until convergence on the standard validation set. Our results,
1639 presented in Figure 17, demonstrate that 1- results from our
1640 main paper replicate under post-pruning fine-tuning, and 2- fine-
1641 tuning procedure creates an independent vulnerability - as after
1642 fine-tuning robustness deteriorates much faster compared to the
1643 standard accuracy vs. pre-fine-tuning results. Figure 18 demon-
1644 strates that the same results apply even when post-pruning fine-
1645 tuning is adversarial (conducted as defined above). These re-
1646 sults are significant for both strengthening the main paper’s con-
1647 clusions, and for showcasing another compressibility-inducing
1648 intervention that leads to structure-induced vulnerabilities.
1649

1650 D.9 EXPLOITATION OF VULNERABLE LATENT DIRECTIONS 1651

1652 Let us consider an MLP with a single hidden layer,

$$g(\mathbf{x}) = \mathbf{C}\phi(\mathbf{W}\mathbf{x}),$$

1653 where ϕ corresponds to the elementwise ReLU function,
1654 and we ignore bias nodes without loss of generality for a
1655 cleaner exposition.
1656

1657 When two such networks have been trained on a dataset
1658 with no regularization vs. strong nuclear norm regular-
1659 ization, we can expect the latter’s \mathbf{W} to have much more
1660 concentrated singular values (SV), i.e. more spectrally
1661 compressible.
1662

1663 Indeed, in Figure 19, we provide a comparison of two such
1664 networks trained on CIFAR-10 (regularization strength 0
1665 vs. 0.05), with hidden layer size 400. We conduct a sin-
1666 gular value decomposition (SVD) of $\mathbf{W} = \mathbf{U}\Sigma\mathbf{V}^\top$, and plot
1667 singular values of \mathbf{W} for both networks $\boldsymbol{\sigma} := \text{diag}(\Sigma) =$
1668 $(\sigma_1, \sigma_2, \dots)$. As in the main paper (Figure 2, left), in the
1669 compressible model the singular values are much more
1670 concentrated, creating the vulnerable directions in ques-
1671 tion.
1672

1673 But what exactly do we mean by attacks “aligning” with
1674 and “exploiting” these directions? For this, let us decom-
1675 pose an adversarial sample: $\mathbf{x}_{\text{adv}} = \mathbf{x} + \mathbf{a}$, where \mathbf{x} is the

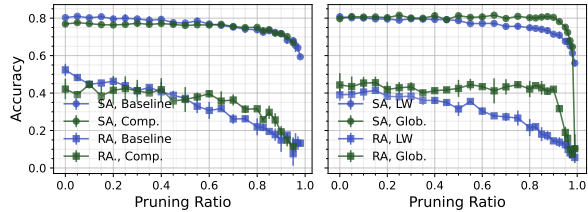


Figure 17: Post-pruning fine-tuning and robustness.

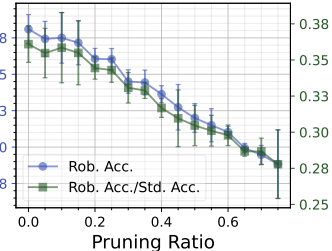


Figure 18: Adversarial post-pruning fine-tuning and robustness.

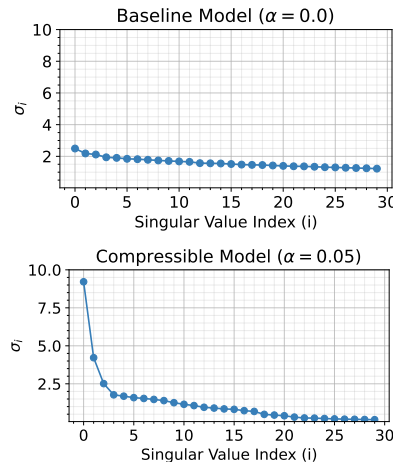


Figure 19: Comparing singular values of a baseline (top) vs. compressible (bottom) model.

1674 clean image and \mathbf{a} is the adversarial perturbation. Examine the pre-activation representation of this
 1675 attack:

$$\mathbf{Wx}_{\text{adv}} = \mathbf{W}(\mathbf{x} + \mathbf{a}) = \mathbf{Wx} + \mathbf{Wa}.$$

1678 Note that for a given sample \mathbf{x} , \mathbf{Wx} , and thus $\|\mathbf{Wx}\|_2$ are fixed. Having a large $\|\mathbf{Wa}\|_2$ (in relation
 1679 to $\|\mathbf{Wx}\|_2$) would make it easier for the attacker to dominate the representation and change the
 1680 downstream prediction.

1681 So, how does the spikier σ in the compressible case help the adversary achieve this? For this, note
 1682 that for every singular value σ_i , there exist the right and left singular vectors \mathbf{u}_i and \mathbf{v}_i , constituting
 1683 the columns of orthogonal matrices \mathbf{U} and rows of \mathbf{V}^\top respectively. So, based on the definition of
 1684 SVD, we can write:

$$\mathbf{Wa} = \mathbf{u}_1\sigma_1\mathbf{v}_1^\top\mathbf{a} + \mathbf{u}_2\sigma_2\mathbf{v}_2^\top\mathbf{a} + \mathbf{u}_3\sigma_3\mathbf{v}_3^\top\mathbf{a} + \dots$$

1685 Without loss of generality, let us assume $\|\mathbf{a}\|_2 = 1$, and examine these terms, $\mathbf{u}_i\sigma_i\mathbf{v}_i^\top\mathbf{a}$. Note that
 1686 given both \mathbf{v}_i and \mathbf{a} are unit vectors, $\mathbf{v}_i^\top\mathbf{a}$ corresponds to *cosine similarity* of the two vectors, a very
 1687 intuitive notion of alignment.

1688 Why would \mathbf{a} “align” with a \mathbf{v}_1 that has a large σ_1 (e.g. as
 1689 in the leading SVs of the compressible model)? To see this,
 1690 let us assume $\mathbf{a} \approx \mathbf{v}_1$. Then, this would mean $\mathbf{v}_1^\top\mathbf{a} \approx 1$, and
 1691 $\mathbf{v}_j^\top\mathbf{a} \approx 0, \forall j > i$. This in turn would imply that

$$\begin{aligned} \|\mathbf{Wa}\|_2 &= \|\mathbf{u}_1\sigma_1\mathbf{v}_1^\top\mathbf{a} + \mathbf{u}_2\sigma_2\mathbf{v}_2^\top\mathbf{a} + \mathbf{u}_3\sigma_3\mathbf{v}_3^\top\mathbf{a} + \dots\|_2 \\ &\approx \|\mathbf{u}_1\sigma_1 + 0 + 0 + \dots\|_2 = \|\mathbf{u}_1\sigma_1\| = \|\mathbf{u}_1\|\sigma_1 \\ &= \sigma_1 \end{aligned}$$

1692 This means that after this layer \mathbf{a} got scaled by this large number
 1693 σ_1 , helping it dominate the representation despite the small
 1694 original attack budget:

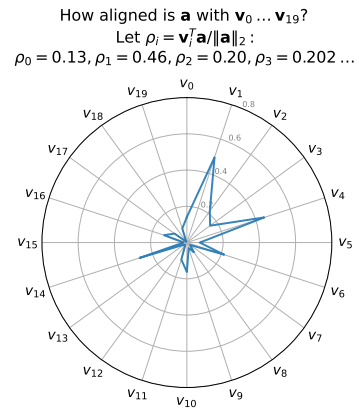
$$\frac{\|\mathbf{Wa}\|}{\|\mathbf{Wx}\|} \gg \frac{\|\mathbf{a}\|}{\|\mathbf{x}\|}.$$

1695 This example makes clear why having a few, very large σ_i as
 1696 a result of compression can create a big vulnerability. Note
 1697 that Nern et al. (2023) also provide complementary theoretical
 1698 justification regarding the dangers of encoders with such potent
 1699 directions.

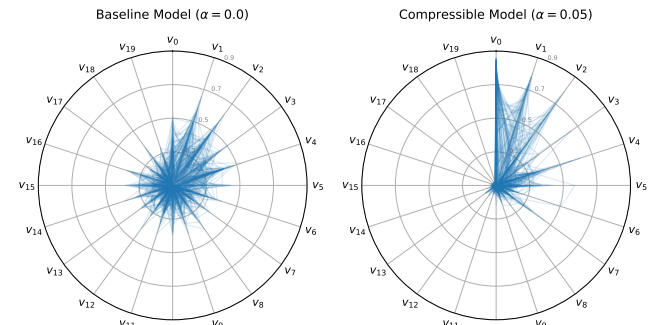
1700 1701 1702 1703 1704 1705 1706 1707 1708 1709 1710 D.9.1 HOW DO SUCH DIRECTIONS GET EXPLOITED IN PRACTICE?

1711 We now move on to the question of whether this actually happens
 1712 in practice. We already established that increased spectral
 1713 compressibility creates vulnerable directions. How can we decide
 1714 whether successful adversarial attacks are actually “exploiting”
 1715 these directions? For any given \mathbf{x} and its perturbation \mathbf{a} , we can
 1716 investigate the “alignment” of \mathbf{a} with every singular direction i , we can
 1717 compute $\rho_i = \mathbf{v}_i^\top \frac{\mathbf{a}}{\|\mathbf{a}\|_2}$, where we
 1718 are now normalizing since \mathbf{a} does
 1719 not have to be unit norm in general.

1720 Note that $\rho_i \in [-1, 1]$ is a measure of alignment between \mathbf{v}_i and \mathbf{a} ; its absolute value $|\rho_i|$ can be
 1721 utilized as a notion of *alignment strength*. An intuitive way to plot this on a radar plot/spider plot. See Figure 20 for an
 1722 example on a single \mathbf{a} . From this graph, we can read that \mathbf{a} mostly aligns with \mathbf{v}_1 , \mathbf{v}_4 , and \mathbf{v}_{14} .



1723 Figure 20: Examining alignment
 1724 of a single adversarial perturbation
 1725 with first 20 singular directions.



1726 Figure 21: Comparing singular directions exploited by
 1727 adversaries in baseline (left) vs. compressible (right) model.

1728
 1729
 1730
 1731
 1732
 1733
 1734
 1735
 1736
 1737
 1738
 1739
 1740
 1741
 1742
 1743
 1744
 1745
 1746
 1747
 1748
 1749
 1750
 1751
 1752
 1753
 1754
 1755
 1756
 1757
 1758
 1759
 1760
 1761
 1762
 1763
 1764
 1765
 1766
 1767
 1768
 1769
 1770
 1771
 1772
 1773
 1774
 1775
 1776
 1777
 1778
 1779
 1780
 1781

We can then use such a plot to understand overall patterns by plotting multiple samples. In Figure 21, we overlay this plot for 100 different samples for both models, for $I = 20$. The results *strongly support* our hypotheses: While the attacks in the baseline model exploit (i.e. align with) all 20 directions, in the compressible model the attacks focus on a few strong, *vulnerable* directions. Then, since the adversaries are using these potent directions at their disposal in the compressible case, we would expect them to dominate the latent representations, compared to the baseline model. Indeed, in Figure 22, we see that this is indeed the case, both for pre-activation ($\|\mathbf{W}\mathbf{a}\|_2/\|\mathbf{W}\mathbf{x}\|_2$) and post-activation ($\|\mathbf{z}_{\text{adv}} - \mathbf{z}\|_2/\|\mathbf{z}\|_2$) representations. Note that these results replicate the results presented in the main paper’s Figure 4, right.

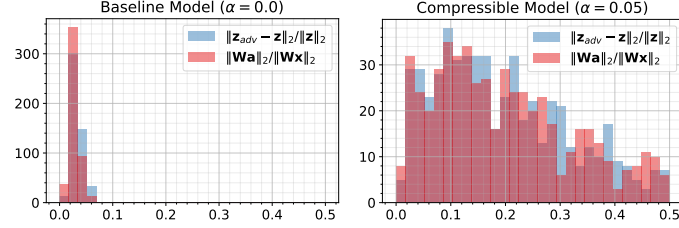


Figure 22: Comparing pre-activation ($\|\mathbf{W}\mathbf{a}\|_2/\|\mathbf{W}\mathbf{x}\|_2$) and post-activation ($\|\mathbf{z}_{\text{adv}} - \mathbf{z}\|_2/\|\mathbf{z}\|_2$) representations of baseline (left) vs. compressible (right) models.

D.9.2 HOW DO WHITE BOX AND BLACK BOX ATTACKS FIND THESE DIRECTIONS?

We now can use this visualization technique to understand the *process of adversarial attacks finding these directions*. We choose two canonical, extensively cited white box and black box attacks for this task respectively: PGD (Madry et al., 2018) and NES (Ilyas et al., 2018).

As a white box attack that assumes access to parameters, PGD is able to conduct iterative first order optimization on the image to find a potent attack direction, projecting back to the ϵ ball after each iteration. Since in a compressible model, aligning with these sensitive directions would quickly increase the loss, the optimization algorithm very quickly finds these directions through its optimization objective. We present the iterates of a PGD perturbation on a single image under the compressible model, see Figure 23 (top). Note that the perturbation quickly aligns with a very strong singular direction, \mathbf{v}_1 ; so much so that by the 6th iteration, the algorithm converged on the attack already.

How can a black box attack make use of these exploitable directions? For this, let us take a closer look at NES. Being a black box attack, NES assumes only access to the logits, prohibiting the use of standard backpropagation. Instead, at every step, NES creates N random Gaussian perturbations and evaluates the loss for all of them. It then calculates a weighted average of these directions (weighted by their impact on the loss) to estimate a *proxy gradient*, and update the adversarial perturbation accordingly. This means that whenever these random perturbations align, even slightly, with any of the exploitable latent directions, they would dominate the weighted average, effectively pulling the estimated gradient toward the vulnerability. So, although not as efficiently, without an explicit knowledge of the parameter space, NES can locate these *adversarially exploitable directions*, just by querying the input space. Indeed, the image in Figure 23 (bottom) presents a direct confirmation of this hypothesis: although it takes many more steps (~ 200) due to the randomness of its perturbations, NES can also converge to exploiting the vulnerable directions in the latent space.

Note that we focused on the ℓ_2 attacks in this exposition; however note that it is quite straightforward to apply a similar analysis to ℓ_∞ case, where the most vulnerable directions are rows \mathbf{w}_k in \mathbf{W} with the largest $\|\ell_k\|_1$.

D.9.3 INTERLAYER ALIGNMENT

Following from previous example, let us now assume a two layer neural network $g(x) = \mathbf{C}\phi(\mathbf{W}^1\phi(\mathbf{W}^0))$ - we will use superscripts to denote the components of layers as well. As a simple example, assume that both layers have a single, very large SV, and rest of their SVs are ≈ 0 . This implies that both have a potent singular direction that can potentially be exploited. However, these directions between layers will need to “align” for their impact to accumulate. More concretely, note that a unit perturbation \mathbf{a} that aligns with the right singular vector of the first layer \mathbf{W}^0 in the input space $\mathbf{a} \approx \mathbf{v}_1^0$ will be “amplified” by σ_1^0 . The resulting output will be in the direction of the left singular vector, i.e. $\mathbf{u}_1^0\sigma_1^0$. Ignoring nonlinearity for now, as large as this intermediate

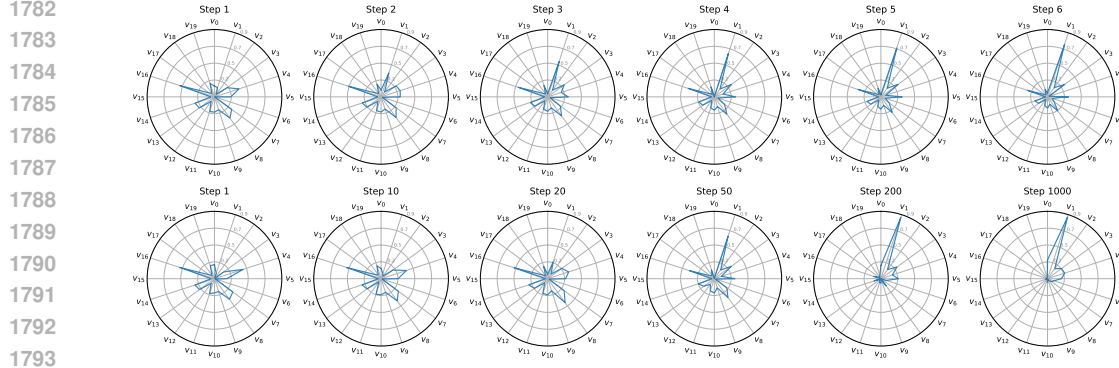


Figure 23: Utilization of singular directions by a white box PGD (top) vs. black box NES (bottom) attack under a compressible model.

representation can be, if it's not in the direction of the next layers' large SV, it will be "quashed". For example, at the extreme end, if $(v_1^1)^T u_1^0 \approx 0$, the attack will effectively disappear before it reaches the final representation and can impact the prediction. This is because in the second layer we will have $\|\mathbf{W}^1 u_1^0\|_2 \approx 0$. So, such a theory will have to take into account how such signals are relayed between layers, while factoring in nonlinearity.

Note that Theorem 3.2 upper bounds L_Φ^p , the p -norm Lipschitz constant of the encoder. This can be computed as the maximum $p \rightarrow p$ operator norm of the Jacobian:

$$L_\Phi^p = \sup_{\mathbf{x} \in \mathcal{X}} \|\mathbf{J}_\Phi(\mathbf{x})\|_p = \sup_{\mathbf{x} \in \mathcal{X}} \|\mathbf{D}^\lambda(\mathbf{x}) \mathbf{W}^\lambda \mathbf{D}^{\lambda-1}(\mathbf{x}) \mathbf{W}^{\lambda-1} \dots \mathbf{D}^1(\mathbf{x}) \mathbf{W}^1\|_p, \quad (81)$$

where the diagonal binary $\mathbf{D}^l(\mathbf{x})$ terms stand for the ReLU nonlinearity. Notice that input dependence of these terms introduce a combinatorial complexity, making it infeasible to directly optimize this term. Our Theorem 3.2, like all other attempts in the literature, utilizes an approximation of this monolith.

Given the that $\|D^l\|_p = 1$, and submultiplicativity of the operator norm, it is possible to write:

$$L_\Phi^p \leq \sup_{\mathbf{x} \in \mathcal{X}} \|\mathbf{D}^\lambda(\mathbf{x}) \mathbf{W}^\lambda \mathbf{D}^{\lambda-1}(\mathbf{x}) \mathbf{W}^{\lambda-1} \dots \mathbf{D}^1(\mathbf{x}) \mathbf{W}^1\|_p, \quad (82)$$

$$\leq \|\mathbf{W}^\lambda\|_p \|\mathbf{W}^{\lambda-1}\|_p \dots \|\mathbf{W}^1\|_p. \quad (83)$$

While this is valid, notice that it corresponds to a very pessimistic assumption: It looks at how much every layer can maximally "stretch" an incoming vector, and multiplies this across layers. This assumes that all "worst case" directions in consecutive layers exactly line up.

Instead, in our bound, while layer operator norms appear (through their compressibility-based decomposition), interlayer alignment terms, $A_p(l) \leq 1$, act as a *correction term*.

$$L_\Phi^p \leq \|\mathbf{W}^\lambda\|_p A_p(\lambda-1) \|\mathbf{W}^{\lambda-1}\|_p A_p(\lambda-2) \dots A_p(1) \|\mathbf{W}^1\|_p. \quad (84)$$

It approximates and factors in how much *dominant directions* actually align in consecutive layers. Every $A_p(l)$ consists of two terms: the main term that computes the alignment of the dominant directions, and a remainder term that goes to 0 as compressibility increases. See Appendix B.5 for how we approximate this (much more manageable) combinatorial computation. We refer the reader to our proofs for a full derivation of these terms. Note that while this term is not the main focus of our paper, Figure 10 includes empirical investigation of this term, and demonstrates that it does not have a strong directional relationship with compressibility.

Utilizing interlayer alignment for regularization. In order to provide a more comprehensive examination of this term, we conduct experiments that test whether this term can be used as another

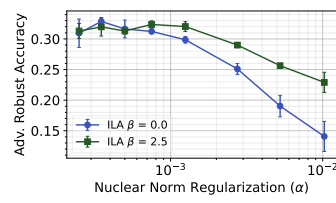


Figure 24: Effects of regularizing interlayer alignment (ILA).

1836 theoretically inspired *intervention for robust compressibility*. With a linear approximation to this term
 1837 (regularizing $\|(\mathbf{U}_k^l)^T \mathbf{V}_k^{l+1}\|_F^2$), we test this hypothesis. Results, presented in Figure 24, are directly
 1838 in line with our predictions: regularizing interlayer alignment between layers lead to a tangible
 1839 increase in robustness under compressibility. While some mild computational hurdles need to be
 1840 addressed for full practical utility, these results both provide a new intriguing research direction for
 1841 robust compression, as well as serving as a yet another confirmation of our theory.
 1842

1843 D.10 COMPARISON WITH ADVERSARIAL PRUNING LITERATURE

1845 As discussed in the main paper, we consider our work to
 1846 be complementary to those in the field of adversarial pruning
 1847 (Piras et al., 2025). To make idea of complementarity
 1848 more concrete, we investigate two structured adversarial
 1849 pruning methods from the literature, and observe an
 1850 intriguing phenomenon. More specifically, our theory im-
 1851 plies that compressibility hurts robustness insofar as it
 1852 increases operator norms and creates adversarially vul-
 1853 nerable directions in the latent space; then can we observe
 1854 successful adversarial pruning methods implicitly control
 1855 operator norms? For this, we investigate HARP (Zhao &
 1856 Wressnegger, 2023) and grouped kernel pruning (GKP)
 1857 (Zhong et al., 2023). We choose these two as they have
 1858 distinct motivating hypotheses, neither of which is in com-
 1859 mon with ours in a meaningful way. We use both papers’
 1860 official repositories to conduct adversarial pruning with
 1861 a ResNet18 on CIFAR-10. As baselines, for HARP we
 1862 train a uniform/layerwise pruning algorithm with standard
 1863 training set, for GKP we replace grouped kernel pruning
 with standard filter pruning.

1864 After the training, we measure the ℓ_∞ operator norms for both methods and compare it to their
 1865 baselines. Intriguingly, as shown in Figure 25, although neither method conducts operator norm
 1866 control *explicitly*, we find that both end up controlling operator norms *indirectly*. Note that this cannot
 1867 just be a by-product of adversarial training as GKP relies solely on filter restructuring, and does not
 1868 involve any adversarial training. We find this to be an exciting first finding towards a comprehensive
 1869 understanding of robust structured compression.

1870 D.11 FURTHER EXPERIMENTS WITH UAEs

1872 We first replicate our original results
 1873 with a ResNet18 trained on CIFAR-10
 1874 in Figure 27. Note that the x -axis in
 1875 this particular figure represents the fix-
 1876 ing of the Frobenius norms to x -times
 1877 their initialization norms - this allows
 1878 us to fix norms using a common value
 1879 for layers that have widely different
 1880 widths (while for FCN we used a sin-
 1881 gle constant). Our results qualitatively
 1882 replicate those in the main paper.

1883 To further probe this causal relationship, we conduct adversarial
 1884 training with ResNet18s under increasing compressibility. Im-
 1885 portantly, we conduct the training either with standard adversarial ex-
 1886 amples vs. UAEs. Given the computational challenges of computing
 1887 UAEs at every iteration, we use the cheaper FGSM attack for uni-
 1888 versal and standard adversarial samples, generated from 0.1 of the
 1889 input batch. Results, presented in Figure 27, illustrate the average
 spread (β) of the dominant terms in the networks under UAE vs.

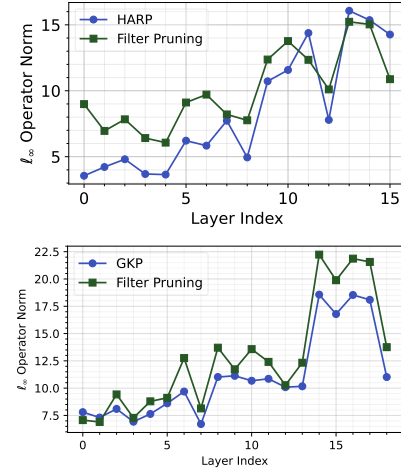


Figure 25: Operator norms of models under adversarial pruning vs. baselines.

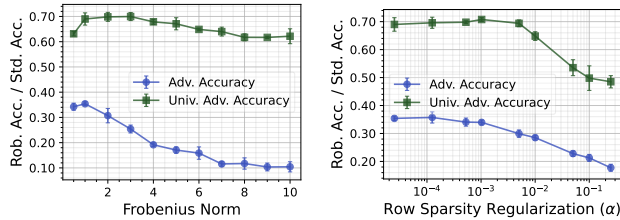


Figure 26: Robustness against standard vs. universal ad-
 versarial attacks under changing Frobenius norm coefficient
 (left) vs. group lasso (right).

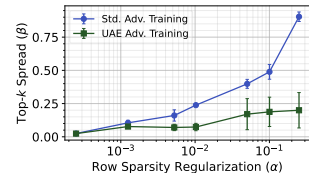


Figure 27: β and UAEs.

1890 standard adversarial training. Our findings show that UAE training dramatically reduces spread of the
1891 dominant terms compared to standard adversarial training, implying that just as creation of vulnerable
1892 latent directions allow UAEs, training against them reduces the potency of such directions, providing
1893 convergent evidence for our hypotheses.

1894

1895

1896

1897

1898

1899

1900

1901

1902

1903

1904

1905

1906

1907

1908

1909

1910

1911

1912

1913

1914

1915

1916

1917

1918

1919

1920

1921

1922

1923

1924

1925

1926

1927

1928

1929

1930

1931

1932

1933

1934

1935

1936

1937

1938

1939

1940

1941

1942

1943